

JGR Solid Earth



RESEARCH ARTICLE

10.1029/2021JB023699

Key Points:

- Unexpected fatal pyroclastic density currents occurred at El Fuego volcano (Guatemala) on 3 June 2018
- Deposit field relations, facies, and thermoremanent magnetization indicate that the block-and-ash flows were deposit-derived
- Collapse of partly hot, perched, unstable tephra accumulations can cause hazardous “deposit-derived PDCs” requiring a new approach to monitoring

Supporting Information:

Supporting Information may be found in the online version of this article.

Correspondence to:

M. J. Branney,
mjb26@leicester.ac.uk

Citation:

Risica, G., Rosi, M., Pistolesi, M., Speranza, F., & Branney, M. J. (2022). Deposit-derived block-and-ash flows: The hazard posed by perched temporary tephra accumulations on volcanoes; 2018 Fuego disaster, Guatemala. *Journal of Geophysical Research: Solid Earth*, 127, e2021JB023699. <https://doi.org/10.1029/2021JB023699>

Received 1 DEC 2021

Accepted 20 MAY 2022

Author Contributions:

Conceptualization: Mauro Rosi, Michael J. Branney

Data curation: Gilda Risica

Formal analysis: Gilda Risica, Fabio Speranza

Investigation: Gilda Risica, Mauro Rosi, Marco Pistolesi, Fabio Speranza, Michael J. Branney

Project Administration: Mauro Rosi

Resources: Fabio Speranza

Supervision: Mauro Rosi, Marco Pistolesi

© 2022. The Authors.

This is an open access article under the terms of the [Creative Commons Attribution License](#), which permits use, distribution and reproduction in any medium, provided the original work is properly cited.

Deposit-Derived Block-and-Ash Flows: The Hazard Posed by Perched Temporary Tephra Accumulations on Volcanoes; 2018 Fuego Disaster, Guatemala

Gilda Risica^{1,2} , Mauro Rosi³, Marco Pistolesi³ , Fabio Speranza² , and Michael J. Branney⁴ 

¹Dipartimento di Scienze della Terra, Università degli Studi di Firenze, Firenze, Italy, ²Istituto Nazionale di Geofisica e Vulcanologia, Roma, Italy, ³Dipartimento di Scienze della Terra, Università di Pisa, Pisa, Italy, ⁴School of Geography, Geology and the Environment, University of Leicester, Leicester, England

Abstract The impact of hazardous pyroclastic density currents (PDCs) increases with runout distance, which is strongly influenced by the mass flux. This article shows that the mass flux of a PDC may derive not only from vent discharge during the eruption, but also from partly hot, temporary stores (accumulations) of aerated pyroclastic material perched high on the volcano. The unforeseen PDC at Fuego volcano (Guatemala) on 3 June 2018 happened c.1.5 hr after the eruption climax. It overran the village of San Miguel Los Lotes causing an estimated 400+ fatalities. Analysis of the facies architecture of the deposit combined with video footage shows that a pulsatory block-and-ash flow flowed down the Las Lajas valley and rapidly waxed, the runout briefly increasing to 12.2 km as it filled and then spilled out of river channels, entered a second valley where it devastated the village and became increasingly erosive, prior to waning. Paleomagnetic analysis shows that the PDC contained only 6% very hot (>590°C) clasts, 39% moderately hot (~200°C–500°C) clasts, and 51% cool (<200°C) clasts. This reveals that the block-and-ash flow mostly derived from collapse of loose and partly hot pyroclastic deposits, stored high on the volcano, gradually accumulated during the last 2–3 years. Progressive collapse of unstable deposits supplied the block-and-ash flow, causing a bulk-up process, waxing flow, channel overspill and unexpected runout. The study demonstrates that *deposit-derived pyroclastic currents* from perched temporary tephra stores pose a particular hazard that is easy to overlook and requires a new, different approach to hazard assessment and monitoring.

Plain Language Summary Pyroclastic density currents (PDCs) are one of the most dangerous things to happen at a volcano: hot mixtures of ash, gas, and rocks travel at high speed across the ground as far as tens of kilometers from the volcano. Shortly after a small eruption of El Fuego volcano (Guatemala) on 3 June 2018, an unexpected pyroclastic current flowed 12 km down a valley, destroying the village of San Miguel de Los Lotes and killing hundreds of people. To understand the cause of this catastrophe, we combined information from satellite photos, the deposits and magnetic data that record the temperature of the rock fragments. Results show that a pulsatory, waxing PDC was generated by the collapse of a perched, unstable accumulation of warm, loose tephra that had built up during the previous few years high on the volcano, from previous small eruptions. The tephra accumulation was rapidly and unexpectedly mobilized late during the 3 June eruption. We propose that this phenomenon represents a new, common type of volcanic hazard that can threaten populations near steep, frequently active volcanoes across the world, and that a different approach to assessment and monitoring is needed to help mitigate this new type of hazard.

1. Introduction

Pyroclastic density currents (PDCs) are flowing mixtures of hot gas and volcanic particles. They are the dominant single cause of fatalities around volcanoes (S. K. Brown et al., 2017) and can be generated by the fountaining of eruption columns, lateral blasts, and growing lava domes (Branney et al., 2021; Druitt, 1998). They transport large volumes of hot, ash-rich pyroclastic debris rapidly across the landscape, and span a wide range of scales, particle concentrations and grain-sizes (Branney & Kokelaar, 2002). A key factor in the hazard they present is the distance they travel (the “runout distance”) over a given topography, and this is significantly affected by the current’s mass flux at the source (e.g., Bursik & Woods, 1996; Shimuzu et al., 2019; Williams et al., 2014). In many cases, it can be assumed that the mass flux of the pyroclastic current derives directly from the vent discharge rate (mass flux) of the eruption (e.g., Roche et al., 2021; Sparks et al., 1997). However, PDCs are known to entrain loose substrate

Validation: Mauro Rosi, Fabio Speranza, Michael J. Branney

Visualization: Gilda Risica, Michael J. Branney

Writing – original draft: Gilda Risica

Writing – review & editing: Mauro Rosi, Marco Pistoiesi, Fabio Speranza, Michael J. Branney

(R. J. Brown & Branney, 2004; Buesch, 1992; Calder et al., 2000; P. D. Cole et al., 1998; Fisher, 1977; Rowley et al., 1981; Sparks et al., 1997; Suzuki-Kamata, 1988; Torres et al., 1996; Wilson, 1985). Erosional entrainment is favored by positive substantive acceleration of the PDC (figure 1.1 of Branney & Kokelaar, 2002) and some possible mechanisms have also been modeled (Farin et al., 2013; Kieffer et al., 2021; Mangeney et al., 2010; Roche et al., 2013). Pyroclast populations in PDCs are typically divided into juvenile, accidental and cognate (Branney et al., 2021). Juvenile clasts commonly dominate volumetrically and are typically erupted close to magmatic temperatures, whereas accidental lithic clasts may be entrained from conduit walls or substrate at lower temperatures and heated within the density current. The proportion of mass entrained in a PDC may vary significantly, and the term *deposit-derived PDC* has been proposed for a PDC that derives mainly from pre-existing tephra deposits rather than directly from vent discharge (Branney & Kokelaar, 2002), such as those derived from hot, loose ignimbrite after the 1991 eruption of Mount Pinatubo (Torres et al., 1996).

Paleomagnetism is commonly used to infer the emplacement temperature of PDCs (Bardot & McClelland, 2000; McClelland & Druitt, 1989; Pérez-Rodríguez et al., 2019; Trolese et al., 2017; Turner et al., 2018; Uheara et al., 2015). The rationale is as follows (e.g., McClelland et al., 2004; Paterson et al., 2010): accidental clasts of volcanic rock entrained from the substrate or conduit walls contain ferromagnetic minerals with a pre-existing magnetic remanence acquired when the rock initially cooled, some time before the PDC under consideration. On subsequent incorporation into a hot PDC such clasts are randomly rotated, reheated, and then deposited in their final position, where they continue to be re-heated as the PDC deposit thermally equilibrates to a temperature that is close to the mean temperature of the initial hot deposit. This reheating erases a portion of the magnetic remanence carried by ferromagnetic grains that have blocking temperatures lower than the temperature of the PDC. The time taken to reach the equilibrium temperature depends on a combination of several factors including size of the clast, deposit volume and temperature, and clast position within the deposit (Zanella et al., 2015 and references therein). As a PDC deposit cools, the clasts acquire a new, partial thermal magnetization, oriented parallel to the local Earth's magnetic field direction at the time of cooling. The resultant clasts may therefore have two magnetic components: a high-temperature component that is randomly oriented because the blocks rotated within the current after having acquired it at source; and a low-temperature component that was acquired later during in situ cooling within the PDC deposit. Different clasts within the same deposit thus share the same orientation of the low-temperature component. The re-heating temperature of each clast is estimated to lie between the highest blocking temperature of the low-temperature component and the lowest blocking temperature of the randomly oriented high-temperature component.

Based on deposit characteristics coupled with paleomagnetic data, this article explores the idea that significant input of loose tephra in a PDC might significantly increase the size of the PDC and lengthen runout distances, thereby increasing the area that is impacted. In a similar way, fast turbidity currents can pick up sediment and self-accelerate or “ignite” (Heerema et al., 2020). We focus on the 2018 disaster at El Fuego in Guatemala because it happened some time after the climax of a 16 km high Subplinian eruption on 3 June (Naismith et al., 2019), and the density current unexpectedly traveled more than 12 km along a valley, overran a village and most of its inhabitants. We aimed to understand how the fatal PDC originated and to account for the large runout distance, with a view to learning about a new and overlooked type of geohazard that concerns many volcanoes, and what might be done to mitigate it.

2. Geological Background

2.1. El Fuego Volcano: Recent Eruption History

El Fuego in Guatemala is a 3,763 m high basaltic-andesite stratocone with steep (30°–40°) slopes. It lies on a volcanic arc close to the Cocos triple junction of Northern American and Caribbean tectonic plates (Figure 1; Álvarez-Gómez et al., 2008; Authemayou et al., 2011; Rose et al., 1978). It is one of the most frequently active volcanoes in Central America with a history of over 50 violent Strombolian and Subplinian eruptions of Volcanic Explosivity Index ≥ 2 since 1524 CE (Berlo et al., 2012; Escobar Wolf, 2013; Global Volcanism Program, 2018; Kurtz, 1913; Rose et al., 2008; Waite et al., 2013). More than 50,000 people live within 10 km of the volcano, and PDCs are a hazard, particularly near the radial valleys (Naismith et al., 2019) and the surrounding vegetated pyroclastic apron.

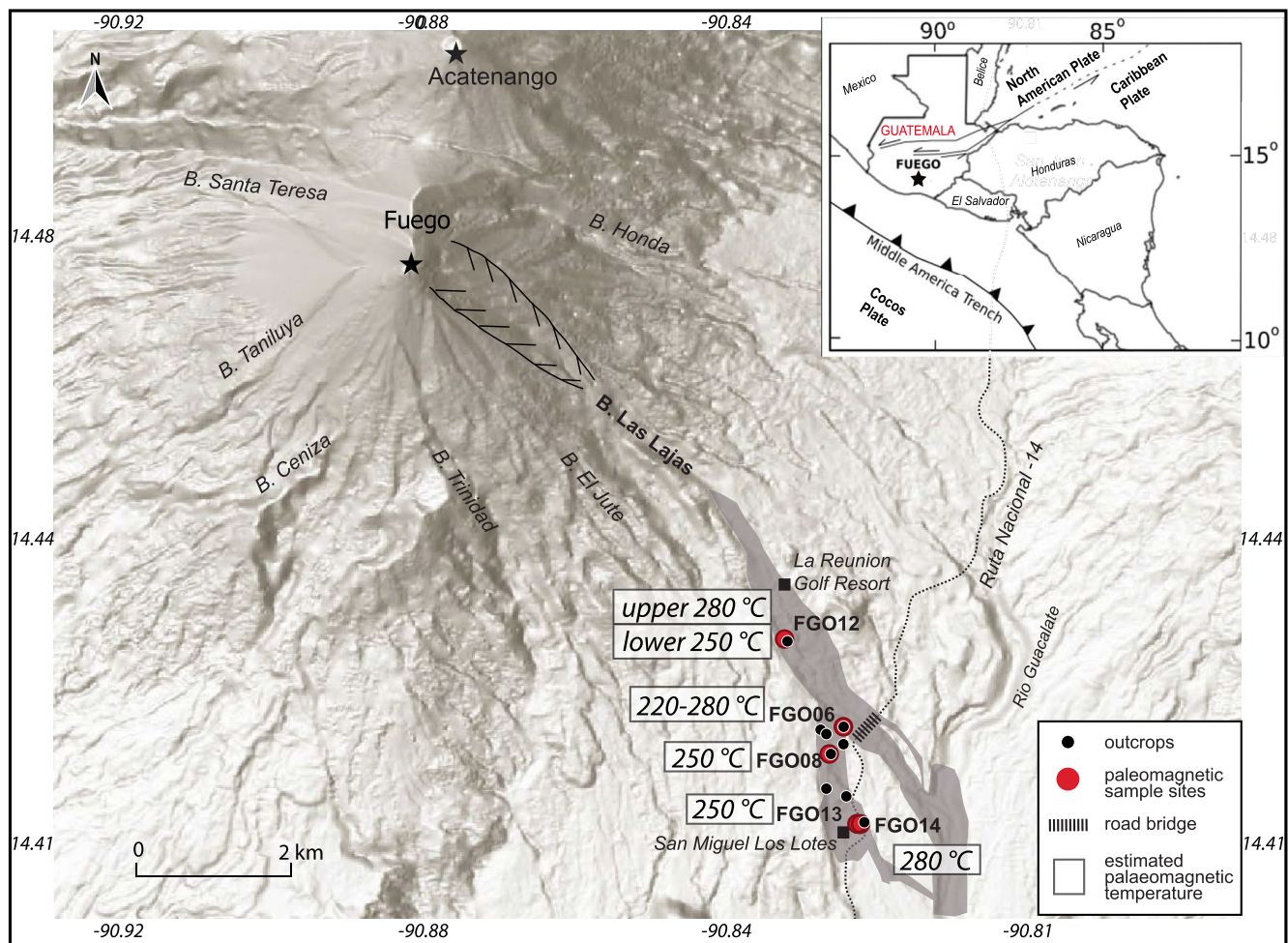


Figure 1. Map of Volcán de Fuego, Guatemala (inset gives location) showing sites mentioned in the text and the small radial valleys, including the Las Lajas valley along which the 24 June 2018 pyroclastic density current (PDC) traveled, destroying the village of San Miguel de Los Lotes. Inset: location; dark gray: the June 2018 PDC deposit; red dots: sample sites; black dots: analyzed outcrops; gray boxes: estimated paleomagnetic temperature; B, barranca (valley).

Since 1999, the eruptions of Fuego have been characterized by periods of persistent degassing, low-intensity Strombolian activity, ash-rich explosions, and lava flows, punctuated by occasional paroxysms (INSIVUMEH, 2012a, 2012b; Lyons et al., 2010; Patrick et al., 2007). Most of the paroxysms have begun with lava effusions and increasing Strombolian activity, climaxing with sustained explosivity, convective eruption plumes, and small PDCs (Naismith et al., 2019).

Between 2015 and 2018, mild to strong Strombolian activity led to the accumulation of ash, lapilli, and bombs on the upper part of the cone, several short lavas flowed into the top of the Santa Teresa and Las Lajas valleys, and PDCs entered the Santa Teresa, Las Lajas, and Trinidad valleys (Figures 1 and 2). Satellite images between 2014 and 2018 (e.g., Figure 2) show new deposits progressively accumulating within and around steep uppermost parts of all the radial valleys, and in particular in the uppermost Las Lajas valley (Figure 2). In 2017, a larger explosive eruption occurred and several PDCs descended the radial valleys, causing the temporary evacuation of local communities.

2.2. The 3 June 2018 Eruption

On 3 June 2018 El Fuego erupted with a Subplinian eruption column and small PDCs along the radial valleys (Naismith et al., 2019). Events presented here are reconstructed based on the volcanological bulletin of Instituto Nacional de Sismología, Vulcanología, Meteorología e Hidrología (INSIVUMEH), and photos and video footage

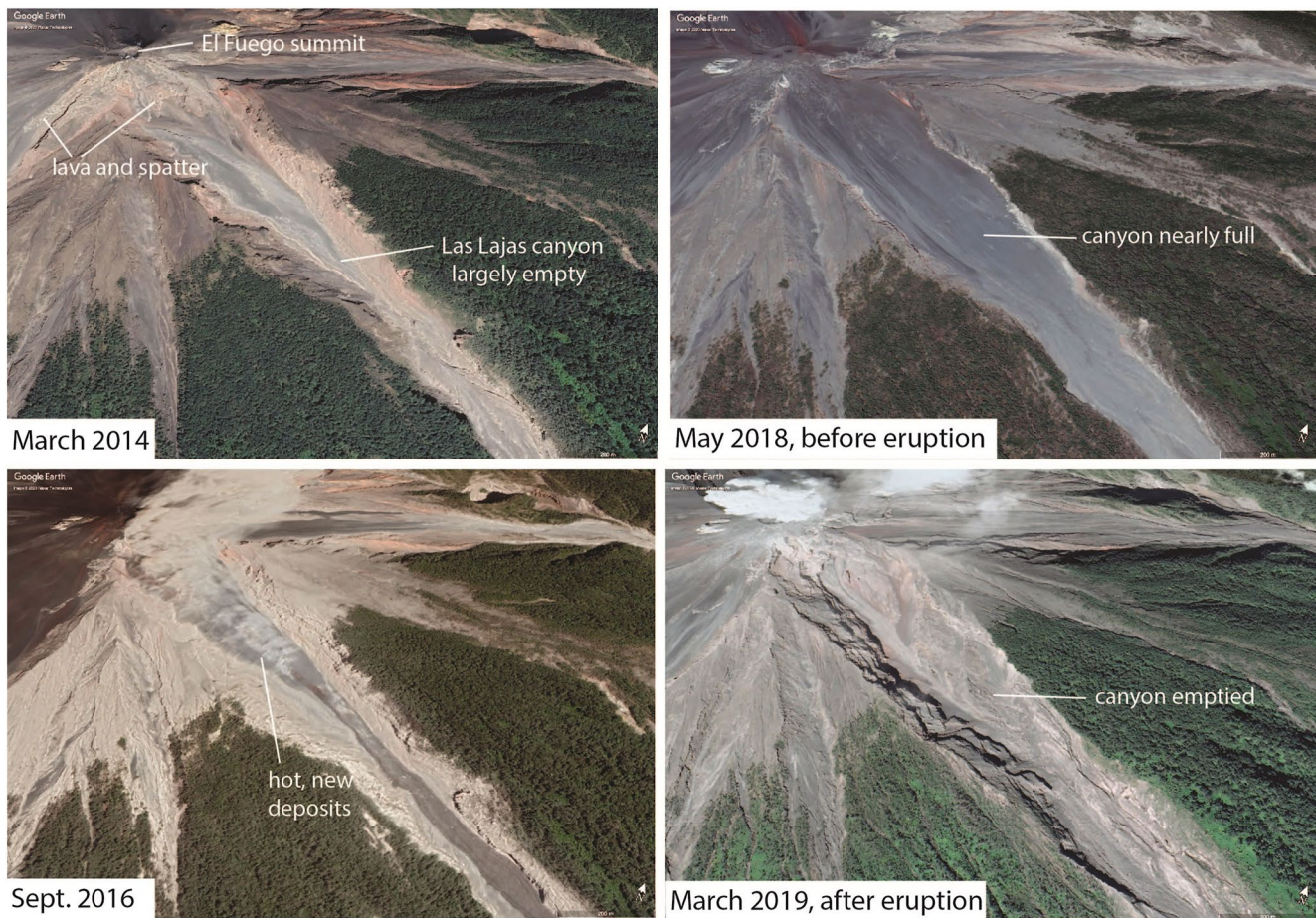


Figure 2. Creation and destruction of a perched, temporary tephra store. Successive Google Earth® satellite images showing the gradual infill of the upper part of Las Lajas canyon around Fuego summit. Fumarolic activity indicates newly emplaced hot tephra in September 2016. The upper canyon is nearly full in May 2018, prior to the 24 June 2018 eruption when it abruptly emptied, exhuming the once buried canyon-wall scarps (March 2019).

recorded by eyewitnesses and reported on the web. Events initially unfolded similar to those of the previous 73 paroxysms (Lyons et al., 2010): the eruption began at 6:00 a.m. local time with strong explosions, loud rumbling, and shockwaves felt by the population. The intensity increased during the morning, and at 10:00 a.m. PDCs were reported in Seca, Santa Teresa, and Ceniza valleys (Boletín Vulcanológico Especial, BEFGO, 28-2018). The explosivity became sustained between 11:30 a.m. and 1:30 p.m., and peaked at 1:10 p.m. with a 16–19 km high Subplinian plume (Pardini et al., 2019). Fallout of coarse lapilli was reported on Acatenango volcano, ~3 km north (Figure 1), between 11:20 and 12:50 a.m. (Boletín Vulcanológico Especial, BEFGO 29–2018; 1'15'' in <https://www.youtube.com/watch?v=uQyMq6BdXSo>). After 1:00 p.m., the size of the eruption plume decreased, but PDCs passed La Reunion Golf Resort (Figure 1) and shortly before 2:00 p.m., PDCs were seen descending into the Seca, Ceniza, Taniluya, and Honda valleys. By 2:24 p.m. a fairly large PDC was filmed descending Las Lajas valley and for the first time reaching the road bridge on Ruta Nacional 14 (Figure 1; 2'06'' in <https://www.youtube.com/watch?v=uQyMq6BdXSo>), filling the river channel below the bridge but leaving the bridge intact. Local smartphone footage from between 2:00 and 3:00 p.m. shows a fresh, fuming PDC deposit by the bridge (<https://www.youtube.com/watch?v=uQyMq6BdXSo>). Between 3 and 3:30 p.m., the top of the volcano was hidden by clouds, and the PDC unexpectedly advanced farther along Las Lajas valley, destroyed the bridge and spilled over both the valley sides and began also to flow southward down a shallow valley to the village of San Miguel Los Lotes (henceforth “San Miguel”) where it buried most of the houses and caused an estimated 400+ fatalities (exact number not known; it is thought that many of the inhabitants were not officially registered). Around 3:09 p.m., the advancing turbulent cloud of ash and gas was filmed descending Las Lajas gorge to the bridge (4'29'' in <https://www.youtube.com/watch?v=uQyMq6BdXSo>). A few minutes later, the pyroclastic

Table 1
Location of the Sampling Sites at El Fuego Volcano, Guatemala and Synthesis of the Estimated Deposit Temperatures

Site code	Latitude, N°	Longitude, W°	N° hand samples	N° cores	Clast type hand samples				Clast type cores				T_{emp} (°C) hand samples	T_{emp} (°C) cores
					GV	GNV	RV	RNV	GV	GNV	RV	RNV		
FGO12	14.431207	90.836831	21 <i>Lw</i>	13 <i>Lw</i>	10	6	5	0	4	7	1	1	250	100/190–220
			21 <i>Up</i>	4 <i>Up</i>	14	4	3	0	0	3	0	1	280	100/310–430
FGO06	14.420898	90.830135	20		14	5	0	1					220–280	
FGO08	14.418387	90.831160	24	10	14	2	7	1	4	2	3	1	250	220
FGO13	14.409516	90.828483	20		11	7	2	0					250	
FGO14	14.409450	90.828187	19		8	9	2	0					280	

Note. Site coordinates were gathered by a Garmin GPS, using the WGS84 datum. N, number of samples. GV, gray vesicular; GNV, gray non-vesicular; RV, red vesicular; RNV, red non-vesicular. *Lw*, lower lever, *Up*, upper level.

current began passing the bridge and visibly waxed, spreading lateral beyond the bridge and overwhelming onlookers on the road hundreds of meters from the bridge, resulting in several casualties. The observed rapid widening of the pyroclastic current across surrounding slopes and along a stretch of road (RN-14) shows that parts of the PDC spilled laterally out of the main alluvial channel. After 3:30 p.m., pyroclastic current activity declined rapidly, although a second atmospheric ash plume, possibly of phoenix type, began at 3:30 p.m. and reached an elevation of 13–14 km a.s.l. Activity ceased after 4:30 p.m.

Satellite images just after the 3 June events show that much of the recent deposit accumulation around the uppermost Las Lajas gorge had disappeared, with the exhumation of older gorge headwall scars at 3,600–2,600 m a.s.l., just below the summit (Figure 2; Albino et al., 2020). Two other radial valleys show evidence of more limited collapse and lack such extensive block-and-ash flow deposits. The 3 June 2018 eruption was the largest eruption of the current eruptive phase, with an estimated total ejected volume of $0.04 \pm 0.01 \text{ km}^3$ dense rock equivalent (Pardini et al., 2019), although this estimate may be an overestimate if it includes recycling of stored, previously erupted tephra. The volume of new PDC deposits in the Las Lajas valley has been estimated to be 0.02–0.03 km^3 (Naismith et al., 2019) and 0.01–0.02 km^3 (Albino et al., 2020), with thicknesses of up to $10.5 \pm 2 \text{ m}$ (Dualeh et al., 2021).

3. Methods

Two weeks duration of fieldwork was undertaken in March 2019 to study the pyroclastic deposits from the 3 June 2018 eruption. Initial focus was on the deposits in Las Lajas valley, close to the La Reunion Golf Resort and San Miguel de Los Lotes village. The fieldwork included facies analysis, logging and photographs at 15 sites (Figure 1), and observations of damage caused to houses and buildings. At the time (March 2019), the deposit was loose and fluvially incised, exposing a range of deposit facies and lateral variations. Pristine fallout tephra was sampled 2.2 km north of the Acatenango summit, where fallout activity was reported during the eruption. The paleomagnetic sampling was based on our observations of facies variations, and was carried out at five representative sites to characterize the magnetization components of clasts.

Paleomagnetic sites (FGO06, 08, 12, 13, 14; Figure 1) were selected in the thicker part of the block-and-lapilli-ash deposit upstream of San Miguel village, from north to south in the Las Lajas valley (see site information in Table 1). One hundred and 52 clasts were collected, most from near the center of the deposit's thickness, which varied widely around an average of c.5 m. To minimize thermal heterogeneity effects, 125 of the clasts were small (1–6 cm in diameter; average c.4 cm), except for one (clast FGO1232; 21 cm in diameter). Twenty-seven larger blocks (7–67 cm diameter, average ~21 cm) were drilled to investigate thermal heterogeneity. Blocks more than a few decimeters in size were avoided, as they can record uneven temperature distributions (Bardot, 2000; Marti et al., 1991). A distinction between juvenile and accidental clasts was not readily evident in the 2018 Las Lajas block-and-ash-flow deposit, so the clast lithologies were grouped into four intergradational field types: (a) gray vesicular, (b) red vesicular (similar but with oxidized surfaces and rare white microphenocrysts), (c) gray non-vesicular, and (d) red non-vesicular. We ascribe no particular genetic origin (e.g., juvenile/accidental or effusive/pyroclastic) to these—the vesicular clasts may simply be textural varieties of the less vesicular clasts. An

additional quantity of clearly recycled alluvial and solidified clasts were not sampled. When sampling clasts by hand, the dip azimuth and dip value of a roughly flat surface of the clast was measured in situ using a magnetic compass and a clinometer (method of Lesti et al., 2011, and Trolese et al., 2017). When sampling by drilling, 2.5 cm diameter cores were drilled using a gasoline-powered, water-cooled portable drill, and oriented in situ by both a magnetic compass and a sun compass. Since a distinction between juvenile and accidental clasts was not evident, all clast types were sampled: 79 were gray vesicular clasts, 23 were red vesicular, 45 were gray non-vesicular, and five were red non-vesicular (Table 1).

Hand samples were cut into 2 cm edge cubes and the drill cores were cut into 1–2 cm long cylinders. To evaluate the temperature differences between the inner and outer parts of the larger (>10 cm) blocks, they were drilled and cores cut into three sections (stubs), and the outer and innermost 1 cm long sections of each core were analyzed separately. A total of 54 specimens from drill cores were analyzed. The thermoremanent magnetization of all specimens was analyzed in the shielded room of the Paleomagnetic Laboratory of the Istituto Nazionale di Geofisica e Vulcanologia in Rome.

Thermal demagnetization of all samples was performed by a Pyrox shielded oven, using 16 demagnetization steps from room temperature up to 590°C (first step was set at 100°C), systematically heating samples for 30 min after having reached rock temperature equilibration. Smaller, 30°C, temperature steps were selected from 100°C to 430°C, and larger 40°C steps for higher temperatures, because the deposit temperature was expected to have been around 200°C–300°C. The first demagnetization step was set at 100°C because the minimum emplacement temperature (T_{emp}) that can be estimated in a 1 yr old deposit of clasts containing SD magnetite and Ti-poor magnetite is ~100°C (Paterson et al., 2010).

Five samples could not be demagnetized at 590°C (FGO0615, FGO0807, 15, 23, FGO1412) and were heated to 640°C. After each temperature step, the natural remanent magnetization (NRM) was measured by a 2G Enterprises DC-SQUID (Direct Current Superconductive QUantum Interference Device) cryogenic magnetometer. After every three steps of thermal demagnetization, the bulk susceptibility was measured with AGICO MFK1 Kappabridge, to evaluate any mineralogical changes associated with the heating. To investigate possible chemical remanent magnetization by post-emplacement growth of secondary magnetic minerals (e.g., Porreca et al., 2008), the variation of the low-field magnetic susceptibility during heating and cooling cycles in air, was measured from room temperature up to 700°C using an MFK1 Kappabridge coupled with a CS-3 furnace, on crushed powders from two specimens per lithological group. Thermal demagnetization data were plotted on orthogonal demagnetization diagrams (Zijderveld, 1967) and on equal-area stereographic projections, and the magnetization components were isolated by principal component analysis (Kirschvink, 1980).

Two approaches can be followed to evaluate the T_{emp} of a PDC: (a) T_{emp} can be regarded as the temperature at which the deposit starts to cool, identified by the lowest re-heating temperature (T_r , i.e., the temperature between the highest blocking temperature $-T_b$ of the low-temperature -LT-component and the lowest T_b of the high-temperature -HT- component) of the sampled blocks (McClelland et al., 2004), or (b) a deposit temperature can be based on the overlap of several T_r due to possible non-uniform cooling in thin PDC deposits, such as near the deposit boundaries (Cioni et al., 2004). We used the approach of McClelland et al. (2004), because we sampled around the middle of deposit sections, collecting several small clasts (<3 cm) to minimize thermal heterogeneity effects.

4. Results

4.1. Deposit Facies Architecture

This section describes the 2018 PDC deposits near the sites where the pyroclastic current interacted with the La Reunion Golf Resort, the road bridge, and San Miguel (Figure 1).

4.1.1. Deposit Shape

The PDC deposit had a ribbon-shape along Las Lajas valley; up to 400 m wide by the golf resort, 200 m at the road bridge, and as much as 400 m at San Miguel (Figure 1). It was thickest (>5 m) in the former fluvial channel and locally pinched out abruptly at steep channel sides, which are up to 10 m high. The deposit top surface formed a gently dipping, slightly convex dip-slope with protruding boulders, local shallow scoured furrows, and low-profile remnant bars and branching distributary lobes already partly modified by post-eruption lahars and

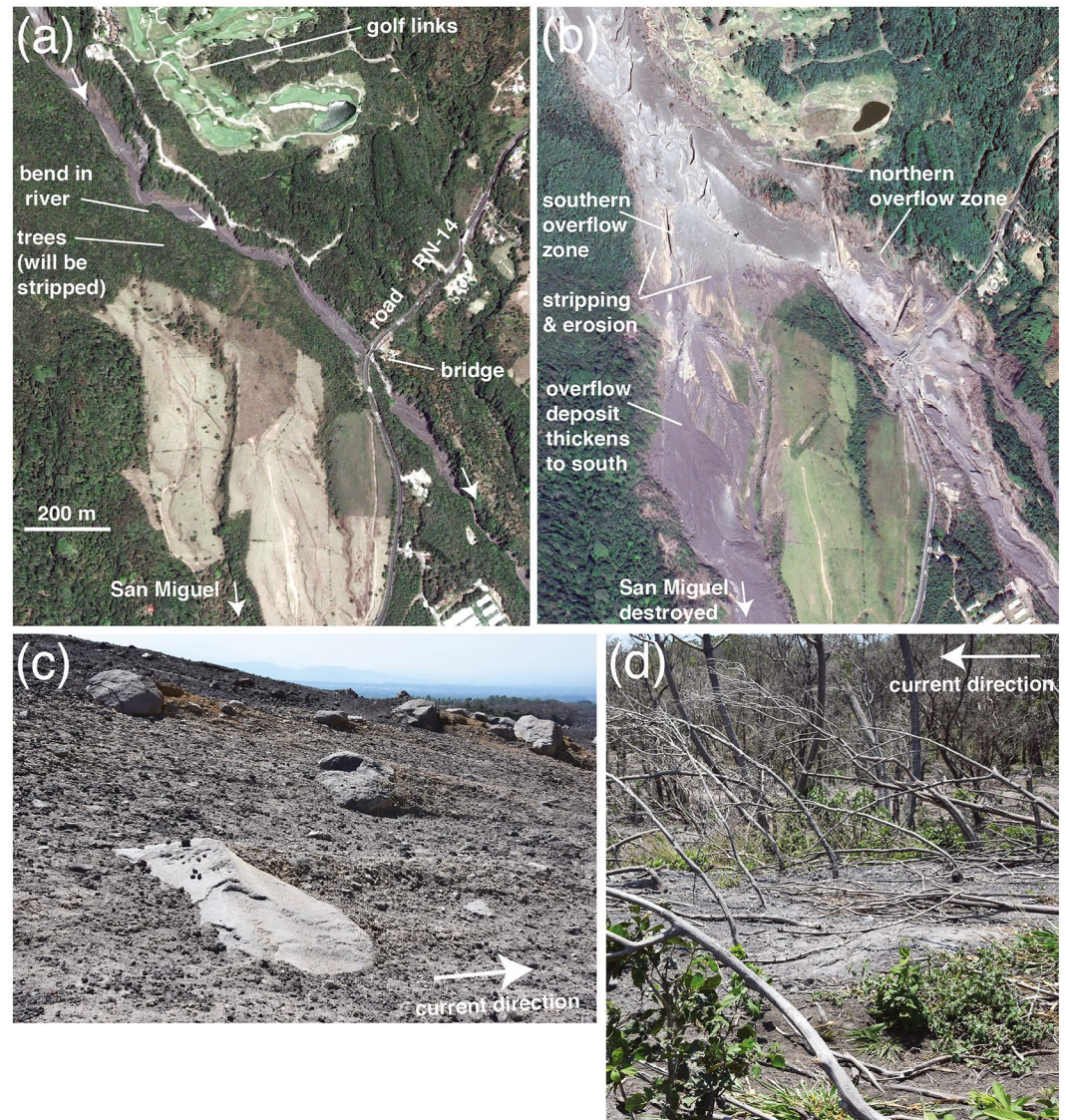


Figure 3. Satellite views (a) before and (b) after the 24 June pyroclastic density currents (PDCs) in Las Lajas valley, showing the destroyed bridge on RN14, and the overspill zones near the golf resort (modified from Google Earth®). A major overspill to the south caused the destruction of San Miguel Los Lotes. (c): Erosional ridges and furrows in the erosional zone where the 24 June pyroclastic current spilled south, stripping forest and substrate soil. (d): Small bayonet trees at the margin of the overspill zone, bent and defoliated by fully dilute parts of the pyroclastic current.

stream wash. Thinner overbank deposits extended laterally from the valley axis, and buried the southern part of the golf resort. Two kilometers south of the golf resort, low interfluvial on either side of the valley had been overridden. This was particularly marked on the south side, on the outer side of a bend in the valley (Figure 3a). There, marked erosional furrowing had occurred to depths exceeding 1 m (Figure 3c), and downstream of this the deposit thickened (Figure 3b) and extended another 2 km south and across San Miguel village.

The overbank deposits generally exhibit the same facies and sorting characteristics as the thicker valley axis deposits although they locally thin to less than 0.5 m.

4.1.2. Block-and-Lapilli-Ash

Most of the deposits were very poorly sorted block-rich lapilli-ash; that is, with abundant scattered angular to subangular blocks and lapilli supported within an ash matrix (Figure 4a). Most blocks were ≤ 30 cm across, but some exceeded 3 m (Figure 4b). Their spacing varied, locally with trains and clusters of 3–8 blocks.

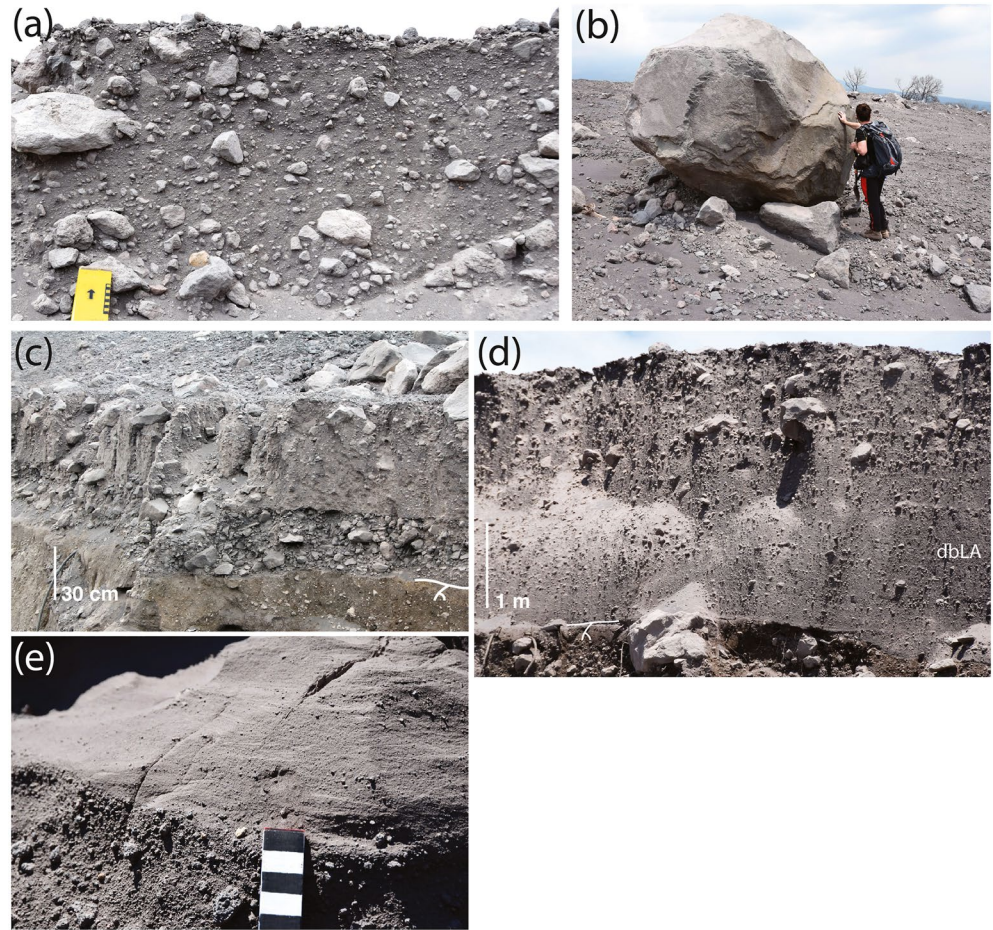


Figure 4. Massive block-and-lapilli-ash deposits from the 24 June pyroclastic density current (PDC) south of the golf resort (Figure 2). (a): Very poor sorting with matrix support, absence of bedding, and minor clusters of clast-supported angular blocks (scale 10 cm). (b): Large 3 m sized blocks at the top of the deposit record “debris-fall” emplacement (sensu Branney & Kokelaar, 2002). (c): Overlying a buried soil (root symbol), a better-sorted lens (<0.6 m thick) of breccia with clast-supported, locally openwork, blocks and lapilli, possibly recording an early levee of the PDC, buried under massive block-and-lapilli-ash as flow conditions waxed. (d): Overall upward-coarsening is common and reflects gradual waxing flow competence. Note subtle, impermanent diffuse bedding. Base is an older, scoured PDC deposit. (e): Normal graded top of the block-and-lapilli-ash is overlain by cross-laminated ash, recording tractional deposition from fully dilute parts (“ash cloud”) of the waning PDC. Scale shows cm. dbLA, diffuse-bedded lapilli-ash.

Upcurrent-dipping imbrication was evident but poorly developed, most clasts being rather equant. The deposit also contained scattered, sub-rounded alluvial boulders, clasts of old soil, and abraded allochthonous trees. It included some better-sorted lenses (<0.6 m thick) of breccia with clast-supported, locally openwork, blocks, and lapilli (Figure 4c).

Parts were massive and non-graded, but subtle to marked inverse and normal vertical grading patterns were common and picked out by the larger clasts (i.e., coarse-tail grading). Many sections showed several variously graded divisions, 5 to >100 cm thick. Both longitudinal and transverse coarse-tail grading is seen across distances ranging from 1 m to >50 m.

The massive block-and-lapilli-ash formed layers <1 m thick (rarely ≤ 5 m axially) with variously gradational to sharp and erosive contacts. Some bed contacts were discontinuous, others could be traced for several tens of meters. Vertical and lateral gradations into diffuse-bedded lapilli-ash were common, as were gradations into layers and lenses of stratified and cross-stratified ash and lapilli-ash. Several sections coarsened upward overall, with an inverse-graded base and some of the largest blocks found toward the top (Figures 4b and 4d). Locally however, the uppermost parts (≤ 50 cm) showed normal-grading and was overlain by fine ash (Figure 4e).

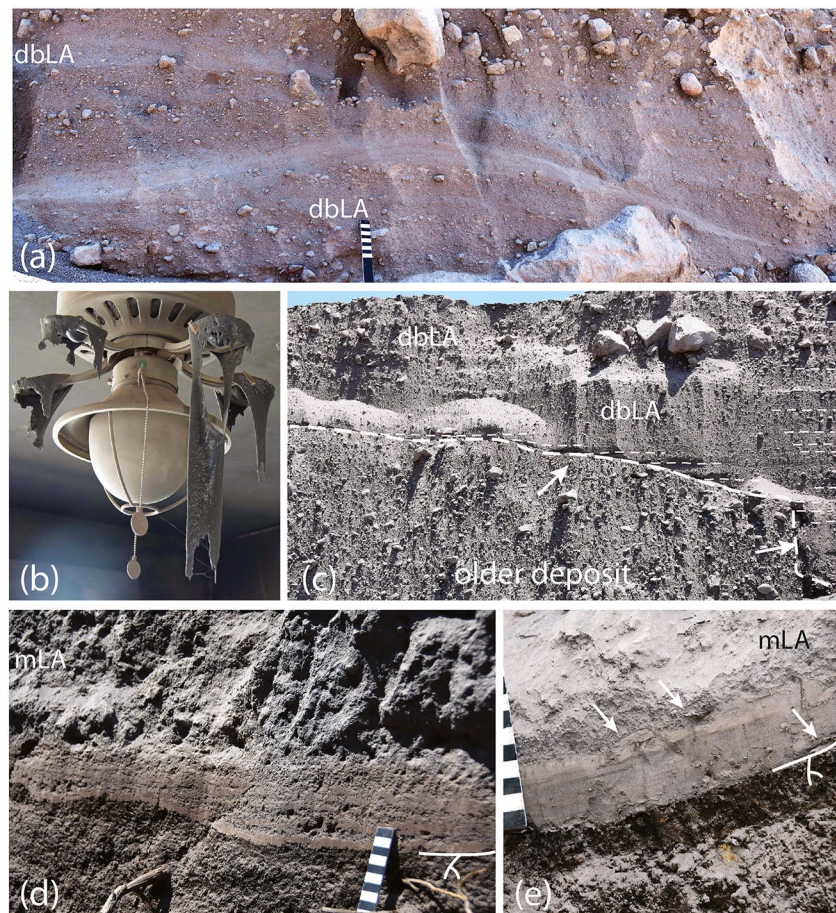


Figure 5. (a): Low-angle aggradational antidune-like bedform with normal and inverse grading, and preservation of both stoss and lee sets in diffuse-bedded lapilli-ash (dbLA) buried by coarsening-upward massive block and lapilli-ash, in the southern overflow zone 2 km north of San Miguel Los Lotes. Current direction left to right. (b): Plastic ceiling fan blades in golf resort melted by heat associated with the brief passage of dilute, upper parts of the pyroclastic current. (c): Buried channel topography (arrows) with onlap of diffuse-bedded coarsening-up block-and-lapilli-ash during aggradation from the waxing, pulsatory pyroclastic current. Near golf resort. (d): Basal parallel and low-angle cross-stratified ash overlain by inverse-graded base of block-and-lapilli-ash records initial ashfalls and turbulent ash clouds prior to the arrival of the granular fluid-based part of the pyroclastic density current. (e): Basal fine laminated ash hosting abundant leaves and twigs (arrows) drapes old soil on channel side. Overlying massive lapilli-ash grades up into the main block-rich facies. (d and e) are from 1 to 2 km North of San Miguel Los Lotes. dbLA, diffuse-bedded lapilli-ash; mLA, massive lapilli-ash.

Low-angle bedforms were locally preserved in the block-and-lapilli-ash (Figure 5a). They showed vertical and lateral gradations from stratified lapilli-tuff to massive block-and-lapilli-ash. Their internal structure records the aggradation and gradual migration of bedforms (antidune or bar-like deposit sand waves) that became buried by block-and-lapilli-ash with inverse grading, presumably as the current waxed. An internal stratigraphy of discrete, longitudinally traceable flow-units was not evident.

Most blocks were non-vesicular to scoriaceous porphyritic basaltic andesite. Some had internal agglutinate textures. A few had prismatic joints and partly detached less vesicular, chilled margins. Rare clasts had white or yellow fumarolic encrustations, others were of old soils. Allochthonous tree trunks, twigs, leaves, and fragments of branches also were common. Some had black, singed exteriors, but interiors of branches more than 6 cm thick were rarely charred. Other evidence for heat was partial melting of plastic cooling fans, light fittings, switches and other electrical housings within buildings of the Golf Resort and San Miguel (Figure 5b). Some of these fittings stood as much as 2 m higher than the top surface of the deposit, and were not abraded, and so the melting can be ascribed to the (brief) current—the upper dilute levels—rather than (prolonged) burial in hot deposit. Rootless phreatic explosion craters and well-developed elutriation pipes were not seen in the locations examined.

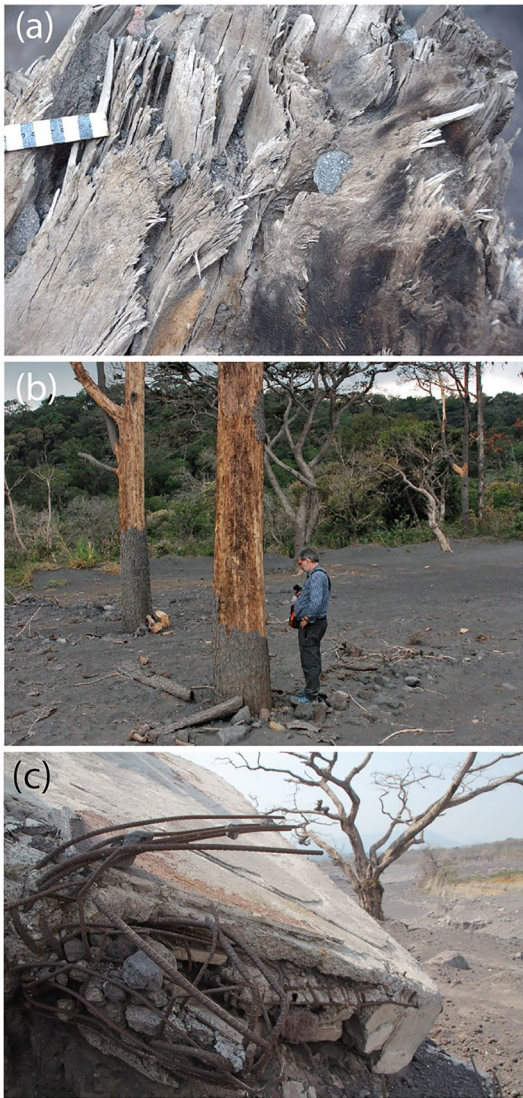


Figure 6. (a): Trees in life position upcurrent of San Miguel Los Lotes were broken off at 1–2 m above the original soil level, suggesting that on 24 June they were initially partly buried by 1–2 m of deposit, and subsequently broken as the flow velocity increased with time. Shredded tree stump shows deeply embedded lithic block and slight charring. Current left to right. (b): Trees standing in flow-marginal deposits close to San Miguel Los Lotes have bark stripped off upper parts by erosion by upper, dilute parts of the pyroclastic current, when lower parts were protected by deposit. (c): Severely shredded reinforced concrete parts of houses that project above the top of the pyroclastic current deposit, golf resort.

4.1.3. Diffuse-Bedded Block-and-Lapilli-Ash

Diffuse-bedded block-and-lapilli-ash was common, with variously distinct and subtle bedding (Figures 4d, 5a and 5c). It showed transitions into both massive and bedded facies. Sorting was very poor and the bedding imper-sistent and subparallel to low-angle, with strata truncations. Local uncon-formable, onlap relationships with the irregular substrate topography showed that the deposition was initially confined to the lowest points on the channel axis, and that the current's depositional footprint then widened over time as the depression progressively infilled with the aggrading deposit (Figure 5c).

4.1.4. Stratified Ash

Thin, discontinuous layers, ≤ 20 cm thick, of fine to medium-grained stratified ash (sensu Branney & Kokelaar, 2002) occurred locally within the lower-most parts of the deposit (Figure 5d), at some lateral margins (Figure 3d), and in uppermost parts of the deposit (Figure 4e). Some contained sparse angular lapilli, either scattered or in short trains. The ash was better sorted than the associated block-and-lapilli-ash layers, being clast-supported and lacking large lapilli and blocks. Contacts with the other facies varied from sharp to gradational. The stratification was an indistinct to well-developed lamination, with variously sub-parallel to discontinuous, lenticular and low-angle cross-stratification, typical of traction deposition. However, well-developed climbing ripples or dunes were absent.

4.1.5. Basal Relations

Thin, fine ash, 1–9 cm thick, was preserved locally along the base of the deposit, particularly at valley sides (e.g., 1 km upstream of San Miguel), where it overlaid the pre-June 2018 soil. It was massive and parallel-lami-nated, and draped steep gully sides (Figure 5e). Locally, this lower ash layer was overlain by low-angle cross-laminated ash about 10–20 cm thick that enclosed lenses, 20 cm long, of coarse ash and lapilli (Figure 5d). This, in turn, was overlain by the inverse-graded base of the main block-and-lapilli-ash deposit (Figure 5d). The basal ash layers and basal part of the overlying massive lapilli-ash contained abundant disarticulated leaves and twigs (Figure 5e). In some places, the basal layer of ash was absent, and the inverse-graded base of the block-and lapilli-ash rested directly upon the pre-2018 soil and (in former river channels) directly upon alluvial gravel. Near the valley axis, there is some evidence of erosional scour, with stripping of the substrate soil, but further from the axis (except at major overbank splays) no erosion was observed and the lower ash lies on the 2018 soil with preservation of flattened but otherwise intact grass. A thin “fines-poor” layer (Branney & Kokelaar, 2002; “ground layer” of; Walker et al., 1981) was not observed.

4.1.6. Relationship With Houses and Standing Trees

At San Miguel, some trees were partly buried by the blocky deposit to a depth of 1–2 m. The buried, lowermost parts were relatively unscathed, whereas higher, projecting parts of the same trees had suffered intense abrasion, with north-facing bark, branches, and foliage ripped off. These same tree trunks had broken off entirely 1–4 m above the level of the old soil, and as much as 3 m above the top surface of the deposit, to leave a pollarded and shredded standing tree stump (Figure 6b). On trees that remained standing, such as near the golf links, severe abrasion persisted to 1.5 m above the top of the deposit, and angular blocks were embedded into the wood up to this height, indicating that during peak flow conditions, blocks had traveled very rapidly at least 1.5 m higher than the surface of the final deposit (Figures 6a and 6b). Younger, thin flexible trees standing 8 m high through thin overbank deposits were bent in

a downstream direction without breaking and partly stripped, similar to “bayonet trees” elsewhere commonly associated with lahars (Figure 3d; Scott, 1988; cf. Guinn et al., 2022), but here due to the PDC.

The damage to houses similarly varied with location. Several houses in San Miguel were buried to a depth of 3.5 m and partly infilled with very poorly sorted, massive to lenticular-bedded block-and-lapilli-ash, rich in tree trunks likely felled from forest upstream of the village. Some of the most intense damage to buildings was found to be near and above the present upper surface of the deposit, where locally even the steel-reinforced concrete has been severely mangled (Figure 6c), testifying to the intense dynamic energy of the current during peak flow conditions.

4.2. Paleomagnetic Results

Thermomagnetic curves generally showed virtually reversible curves, except for the gray, non-vesicular samples, which yielded lower susceptibility values on the cooling curves (Figure S1 in Supporting Information S1). Almost all samples had Curie temperatures around 580°C, indicating the presence of magnetite. A few showed an inflection in the heating curve near 450°C, which indicates that these few additionally contained minor titanomagnetite. Bulk volume susceptibility values ranged between 5.5×10^{-2} and 1.0×10^{-1} SI, with no significant changes during heating, implying there were no significant transformations of magnetic mineralogy. NRM intensities of all clasts range from 2×10^{-3} to 140 A/m (17.8 A/m on average). The demagnetization patterns fell into three groups (Figure 7).

4.2.1. Group 1: Clasts With a Single Component Subparallel to the 2018 Geomagnetic Field Direction

These clasts show only one magnetic component until the demagnetization was complete (generally at 590°C; Figure 7a), and are inferred to have been hotter than 590°C, the Curie temperature of magnetite, at the time they were deposited by the Las Lajas density current. Only ~6% of all samples (of which ~66% of the hand specimens and ~33% of the drill cores) belong to this group.

4.2.2. Group 2: Clasts With Both Low- and High-Temperature Components

These samples yielded two straight-line segments in the orthogonal plot (Figure 7a), corresponding to two magnetization components: an HT component that represents the original magnetization directions acquired before the eruption, later randomized in the density current; and an LT (from 100°C to 510°C) component that records a younger partial thermoremanence subparallel to the 2018 Earth's magnetic field (Figure 8). A few of these clasts (9 hand specimens and 2 cores) show two HT components. In some, the HT and LT components are separated by a curved path and the T_i is taken to lie in the temperature range between the highest T_b of LT component and the lowest T_b of HT component. About 39% of all the samples (of which 82% of the hand specimens and 18% of the drill cores) belong to Group 2.

4.2.3. Group 3: Clasts With a Randomly-Oriented High-Temperature Component

These clasts did not start demagnetizing until reheated to 250°C–500°C, and only one randomly oriented HT component could be isolated (Figure 7a). These clasts are thought to have been colder than the lowest T_b of the HT components isolated, and they did not acquire an LT component sub-parallel to the local geomagnetic field as they did not contain ferromagnetic grains with low temperature (LT) T_b spectra (Figure S2 in Supporting Information S1). Thus, the lowest T_b of the HT component simply indicates an upper boundary of the possible clast temperature range. About 51% of all samples (of which ~83% of the hand specimens and ~17% of the drill cores) show this pattern.

Five samples (~3%) showed scattered demagnetization paths and were discarded from further consideration.

In the drilled larger blocks, comparison between the T_i of the internal and external parts was instructive (Figures 7b, 9 and 10). In four blocks, the central part was hotter than the outer part (430°C vs. 310°C in red non-vesicular block FGO0831; Figure 7b), whereas in two other blocks the core was colder than the outer parts (e.g., completely cold core vs. 310°C outer part, for gray vesicular block FGO1252, Figure 7b). This demonstrates that the PDCs entrained some completely cold blocks and that these were partly heated up by the density current and/or within the block-and-ash-flow deposit as it started to thermally equilibrate (the block cores remaining cold); and also included some hot (400°C–500°C) blocks, the outer parts of which cooled to 310°C at the equilibrium temperature within the final deposit (the two examples shown).

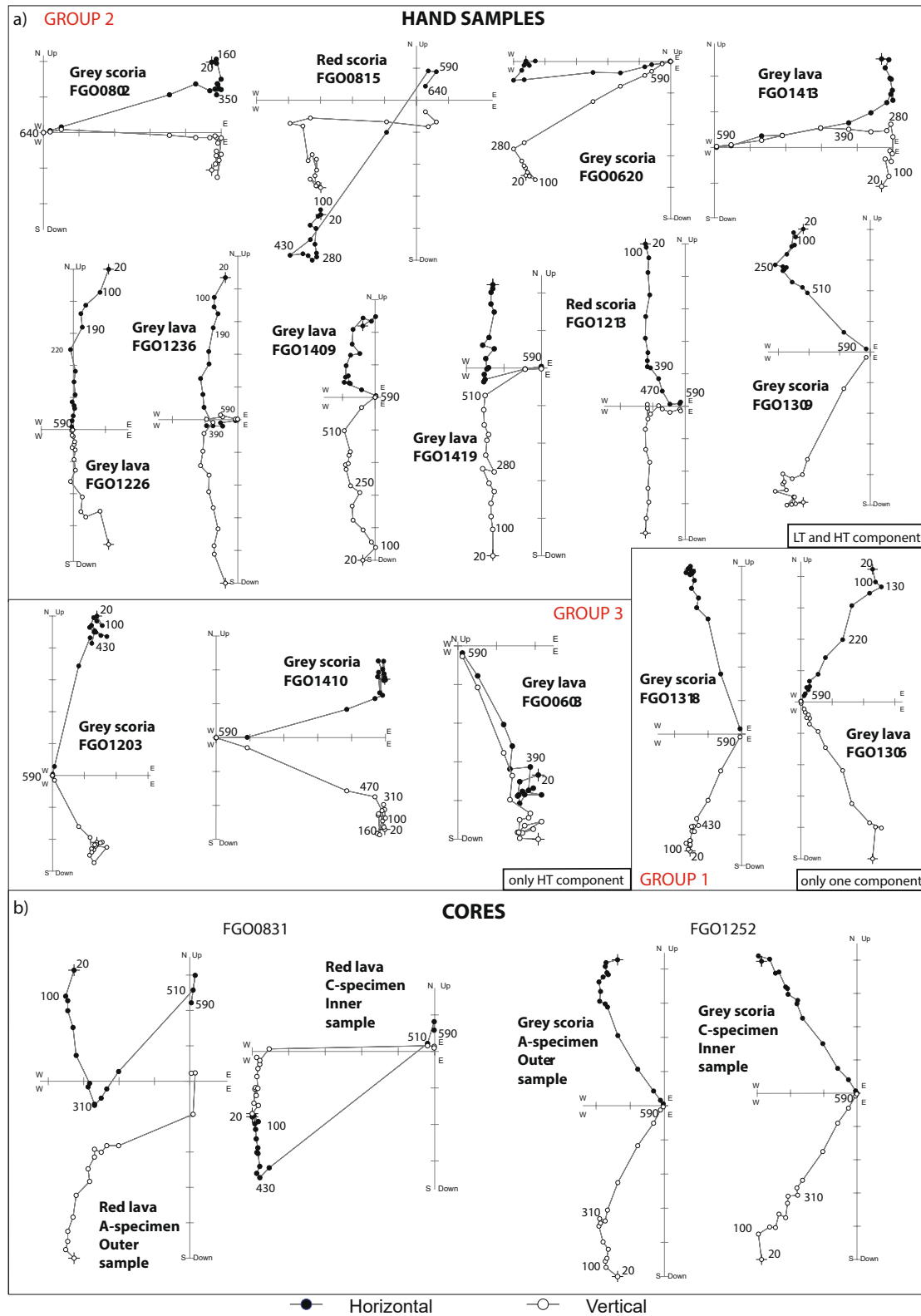


Figure 7. Representative orthogonal vector diagrams of typical demagnetization data, in situ coordinates. Filled and empty dots represent projections on the horizontal and vertical planes, respectively. Demagnetization step values are in °C. (a) Hand samples. (b) Drilled cores from big blocks. A-cores and C-cores represent the outer and inner core specimens respectively.

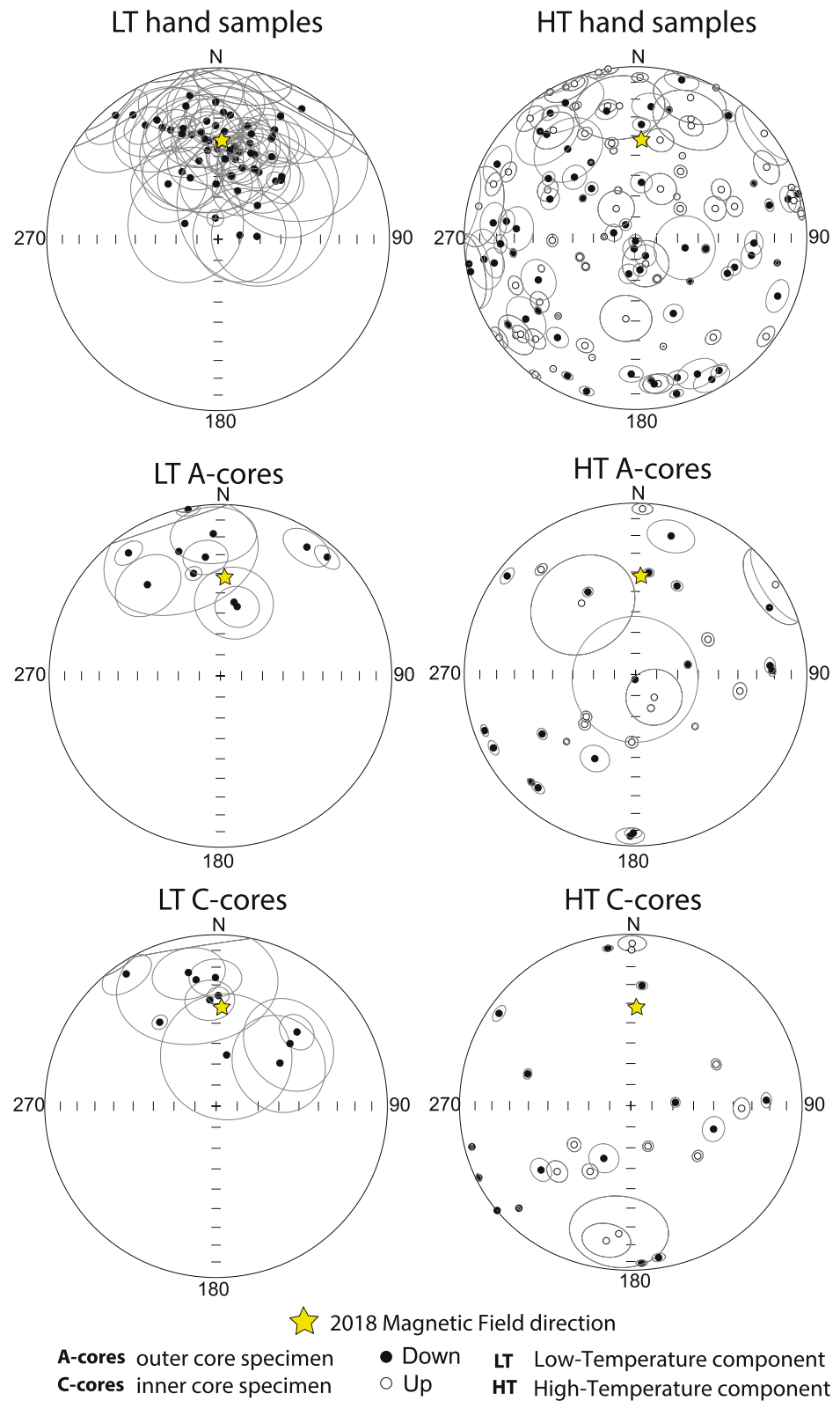


Figure 8. Equal-area projection of high temperature (HT) and low temperature (LT) magnetic components of clasts from the June 2018 Las Lajas PDC deposit, in situ coordinates. Yellow stars indicate the 2018 local geomagnetic field direction (IGRF model, 3 June 2018). The ellipses around the paleomagnetic directions are the projections of the relative maximum angular dispersion values.

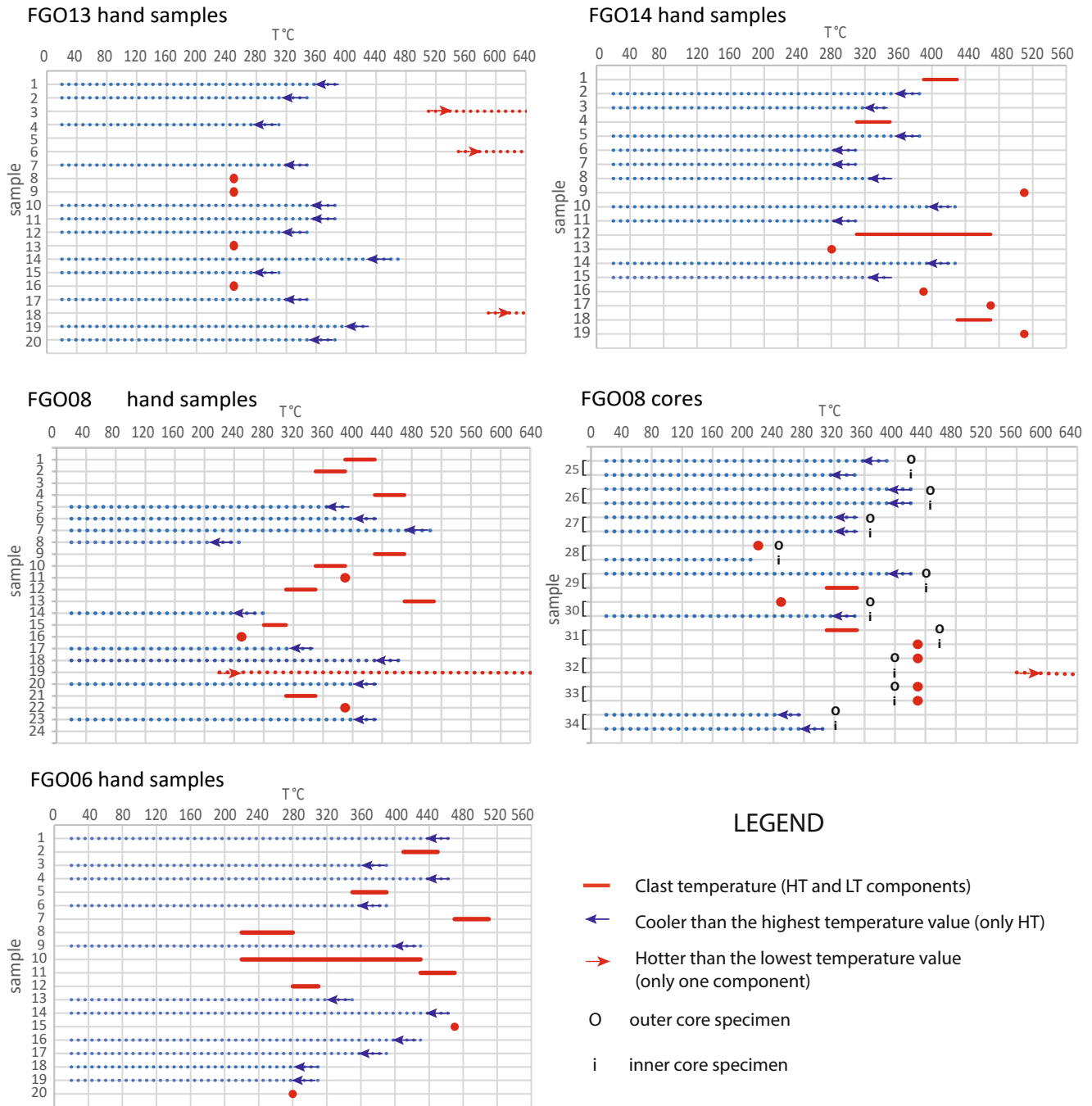


Figure 9. Paleomagnetically inferred re-heating temperatures of FGO06-13-14-08 sites. Red lines represent the temperature range (HT and LT components). Blue arrows represent clasts with only randomly oriented HT components (only upper bound temperatures can be deduced). Red arrows represent clasts with only one component subparallel to the 2018 local geomagnetic field direction (only lower bound temperatures can be deduced). O and I indicate outer and inner core rock slices, respectively.

Orientations of the LT and HT components are shown on equal-area stereographic projections (Figure 8). The mean direction of all LT components ($D = 3.5^\circ$, $I = 44^\circ$, $\alpha_{95} = 5.8^\circ$) is consistent (considering its 95% confidence cone) with the local geomagnetic field direction for the 2018 year at El Fuego volcano ($D = 1.2^\circ$ and $I = 42^\circ$, IGRF model <https://www.ngdc.noaa.gov/geomag/calculators/magcalc.shtml#igrfwmm>), while the HT components are randomly oriented ($k = 1.13$ and $\alpha_{95} = 35.1^\circ$).

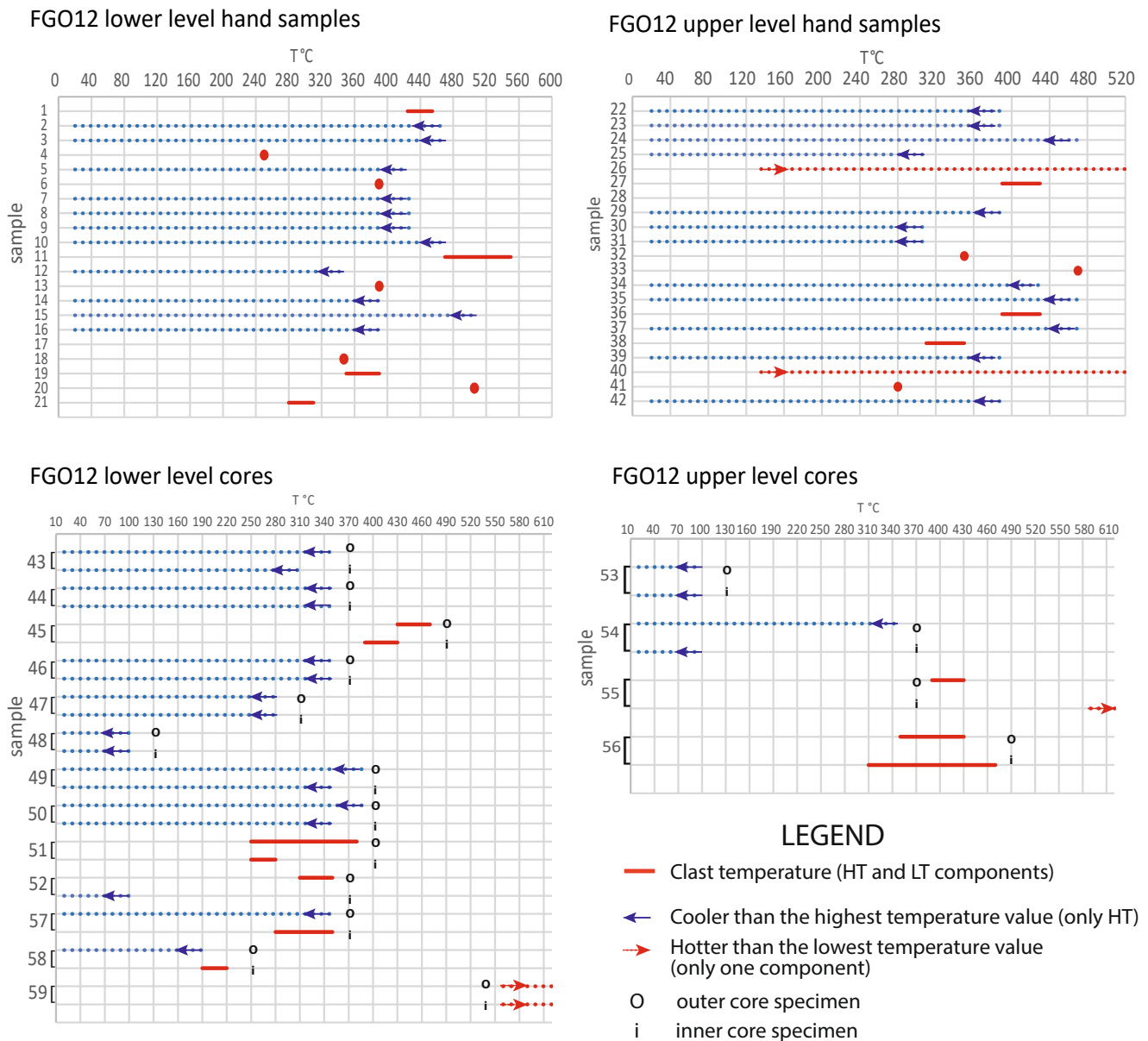


Figure 10. Paleomagnetically inferred re-heating temperatures from site FGO12 (Figure 1). Red lines represent the temperature range (HT and LT components). Blue arrows represent clasts with only randomly oriented HT components (only upper bound temperatures can be deduced). Red arrows represent clasts with only one component subparallel to the 2018 local geomagnetic field direction (only lower bound temperatures can be deduced). O and I indicate outer and inner core rock slices, respectively.

Temperatures for each sample are given for Groups 1–3 based on the magnetic components (Figures 7, 9 and 10) and according to lithologic type (Figure S3 in Supporting Information S1). Generally, the hand-specimens record temperatures between 200°C and 500°C, with a cluster between 300°C and 480°C, and few samples record LTs, between 240°C and 300°C. Only a few Group 1 clasts occur, and display $T > 500^\circ\text{C}$. One shows $T > 220^\circ\text{C}$, implying a 220°C Curie temperature, likely from titanomagnetite. Internal parts of all the large blocks display similar characteristics, with some hot blocks recording 400°C–500°C, some hotter than 550°C, and few recording LTs of 100°C–240°C, which probably reflect thermal disequilibrium of large, cold clasts that were not heated to a deposit thermal equilibria temperature. Most of the drill cores displayed similar temperatures in the inner and outer sections, except for four (FGO0831–32, FGO1255–58), and two cores (FGO1245–51) in which higher temperatures were observed in the inner and outer rock slices, respectively.

To evaluate the T_{emp} the lowest T_r found on each site was considered (McClelland et al., 2004). Sampling at different levels in the Las Lajas deposit provided evidence that T_{emp} s increased with time. Both at San Miguel (FGO13; Figure 1) and near the golf resort (FGO12 lower), hand samples in the lower parts of the deposit indicated a T_{emp} of 250°C, whereas those in upper parts (FGO14 and FGO12 upper) of the deposits indicated T_{emp} of 280°C (Figures 9 and 10). The proportion of hot clasts also increased with height in the deposit. From these data, we infer that during the deposition at these sites, the T_{emp} of the block-and-ash flow waxed by ~30°C. Several of the larger blocks were not used in this analysis, because they did not thermally equilibrate.

Overall, the results suggest that hand sampling of 2–3 cm clasts yielded a better temperature estimate than drilling larger (decimeter sized) blocks, because large blocks, both hot and cold, did not reach thermal equilibrium before the deposit finally cooled. The 2–3 cm sized clasts thermally equilibrated more readily and may more faithfully represent the deposit temperature. There was no clear correlation between magnetic temperatures and lithology (Figure S3 in Supporting Information S1). Clasts recording the highest temperatures (>590°C) are all gray (37% vesicular; 63% non-vesicular) whereas those recording temperatures of 200°C–540°C are varied (59% gray vesicular; 20% gray non-vesicular; 4% red non-vesicular; 17% red vesicular); and cold clasts (<200°C) are mainly non-vesicular (75% gray; 25% red).

5. Discussion

5.1. Interpretation of Clast Thermal Histories

Clast groups 1, 2, and 3 are inferred to have contrasting thermal histories. The Group 1 clasts must have been at $\geq 590^\circ\text{C}$ during transport and deposition by the Las Lajas block-and-ash flow because they all record the same geomagnetic field direction, acquired during in situ cooling within the deposit. It is unlikely that the deposit was hot enough to have heated them up, since the other (Groups 2 and 3) clasts in the same deposit record lower temperatures (200°C–300°C).

Group 2 clasts have randomly oriented, HT components that therefore must have been acquired prior to entrainment by the June 2018 PDCs. They also had an additional lower-temperature magnetic component that clusters around the 2018 geomagnetic field direction (Figure 8) and so indicates a thermoremanence overprint acquired in situ within the deposit. The few (8%) of Group 2 clasts with two HT components (e.g., FGO0815 in Figure 7a) probably acquired both of them within proximal tephra accumulations high on the volcano; the first one was acquired followed a small rotation due to a gravitational adjustment within the still hot and loose accumulation before the second HT component was acquired as cooling at that site continued, this all before the clasts were transported in the June 2018 PDCs. They then acquired the LT component after PDC emplacement while they finally cooled in situ within the PDC deposit.

Group 3 clasts did not demagnetize until heated to medium and high temperatures (HTs; 250°C–500°C), so they likely contain magnetic grains of similar size or composition and almost no magnetic grains with low-intermediate unblocking temperatures (possibly magnetite and Ti-poor magnetite; e.g., R. P. Cole et al., 2019). For these samples, it is not possible to identify a clear T_r . Only three cores in this group recorded a very low T_r (<100°C): these were drilled from 15 to 12 cm diameter blocks that were probably not heated homogeneously by the PDCs, and failed to reach thermal equilibrium (e.g., Porreca et al., 2008).

5.2. Source of the PDCs From Thermal Data

We have established from video and photo footage recorded by eyewitnesses available on the web and deposit characteristics that the event that destroyed San Miguel was a block-and-ash flow. However, only 6% of clasts in the deposit were transported very hot (>590°C) and are thought to have erupted as juvenile clasts during or shortly before the June 2018 eruption. Thirty-nine percent of the clasts were transported moderately hot (average 410°C; range 300°C–500°C) and were probably erupted weeks and months before 3 June 2018, and stored temporarily in and around the head of Las Lajas valley (Figure 2), where they had started to cool prior to 3 June. Another 51% of the clasts (of which 4% recorded temperature <200°C) were transported cool, and presumably derived from cooler (i.e., older) materials within the perched tephra accumulation in and around the head of Las Lajas valley prior to the main block-and-ash flow. Overall, these proportions are consistent with the block-and-ash flow's mass being derived mostly from a temporary store (accumulation) perched around the summit

of the volcano and upper part of the Las Lajas gorge. Satellite photos (Figure 2) show the overall accumulation of pyroclastic materials during the period 2015–2018. Much of this material was loose, and the visible textures and morphologies of the surface of the perched tephra store are consistent with emplacement by granular flows. Some of the stored tephra was clearly very hot during its accumulation as indicated by abundant fumaroles in the perched deposits (Figure 2) and was probably emplaced as grain flows or small, proximal PDCs. The temperature of a clast stored in the upper part of Las Lajas gorge would depend upon its size, initial temperature (e.g., fallout lapilli and ash likely cool, some ballistics and PDC deposits may have been hot), its duration of residence and its location within the store; for example, a clast at the top surface or feather-edge of the deposit cools more rapidly than a clast deeply buried in a warm interior. Near-vent deposits in 2015 and early 2018 appear to include layers of spatter and proximal lavas.

A proportion of the cold clasts in the 3 June block-and-ash flows may have derived from canyon walls, alluvial gravels and old PDC deposits along the Las Lajas valley. This is consistent with the erosion surfaces, and rounded alluvial boulders and soil fragments in the block-and-ash-flow deposit. Group 3 includes clasts for which temperatures between 200°C and 300°C cannot be excluded, as the thermoremanent magnetic data do not form a unique cluster (Figures 9 and 10). However, some of the large blocks were definitely cooler than 100°C.

5.3. Interpretation of Deposit Facies Architecture, and Inferred PDC Dynamics

5.3.1. Mode of Emplacement

Several features of the June 2018 deposits are characteristic of emplacement by a PDC. These include: (a) the topographic control (along the Las Lajas valley), (b) the very poor sorting, (c) the coarse-tail type of grading, (d) the evidence for $T_{emp} > 100^{\circ}\text{C}$ (paleomagnetic data; charred wood; melted plastics; reports of eye-witnesses and rescue teams called to the disaster), and (e) the close association of coarse, matrix-supported deposits with subordinate, thin stratified ash layers. The latter association arises because many granular-fluid-based PDCs (Branney & Kokelaar, 2002) are markedly density-stratified with a high-concentration granular dispersion (in which grain interactions dominate) at lowermost levels, from which the very poorly sorted, more massive layers are deposited; and more dilute, higher levels, in which ash is carried in turbulent gaseous suspension (Breard & Lube, 2017; Kelfoun, 2017). Only where the dilute turbulent levels locally impinge directly upon the ground surface (such as before and after the passage of the lower granular dispersion, or to the side of it) does traction sedimentation occur, with the formation of stratified ash: at such locations, the currents are inferred to have been dilute and turbulent right down to the base (i.e., “fully dilute PDC” of Branney & Kokelaar, 2002; this is sometimes called an “ash-cloud surge” although it is part of the same PDC and may be sustained; Breard & Lube, 2017). That emplacement was by a pyroclastic current is further confirmed by the nature of the stratification in the thin ash layers, which is predominantly low-angle to subparallel and discontinuous, rather than rippled. This is typical of tractional deposits from fully dilute parts of a hot PDC that moves too rapidly for the development of ripples: in aqueous currents (e.g., waning turbidity currents; Jobe et al., 2012) velocities typically decelerate sufficiently to form ripples, whereas in fully dilute PDCs thermal lofting can intervene before the deceleration is sufficient to form ripples. Thermal lofting was witnessed on 3 June at Las Lajas.

5.3.2. Flow Pulsing and Waxing

The duration of the main Las Lajas PDC lasted substantially less than c.1.5 hr. Fluctuating flow conditions with repeated pulses (rapid waxing then waning mass flux) are recorded in the block-and-ash deposit by the diffuse internal layering with patterns of vertical, inverse, and normal coarse-tail grading (Figures 5a and 5c). There is little evidence for the main Las Lajas event being a succession of separate, small single-pulse flows. Some temporary cessations of flow likely occurred, as witnessed between 2 and 4 p.m. by the RN-14 bridge, but most were probably short-lived and local in that downcurrent-traceable, stacked massive flow-units with interdigitating ashfall layers recording general hiatuses between flows were not seen. Rather, the laterally impersistent grading patterns, the vertical, lateral and downcurrent transitions from massive into diffuse-bedded packages, the numerous lateral thickness changes, and the preservation of aggradational bedforms (e.g., Figures 5a and 5c) are thought to indicate a predominantly sustained and braided, but fluctuating, granular-fluid-based PDC of limited duration, at the base of which ephemeral constructional bars, levees or antidune-like sand waves rapidly formed, shifted and became buried within the aggrading deposit.

The well-sorted lenses, ≤ 60 cm high, of openwork clast-supported clasts (Figure 4c) are interpreted as short-lived granular levees and dams (e.g., Johnson et al., 2012) that were rapidly buried as both the flow width and the runout distance of the block-and-ash-flow increased as flow conditions waxed (e.g., Branney & Kokelaar, 2002; Rocha et al., 2019). Additional evidence for overall waxing flow includes: (a) the overall upward-coarsening of the deposit at many sites; (b) the film footage showing that the pulsing current gradually advanced further and further along the valley with time; (c) the overlap relations in the valley-confined deposit that record broadening of the area of deposition with time; (d) the evidence with height on trees and houses at San Miguel, that initially, when the block-and-ash flow arrived at the site, it buried the lowermost parts of obstacles relatively passively during less vigorous earlier phases, which were followed by peak flow conditions in which maximum dynamic pressure caused erosion and bulldozing of unprotected upper parts of the obstacles (Guinn et al., 2022); (e) the delayed destruction of the road bridge, some time after the current first reached it; and (f) the footage showing that the PDC was initially channelized, and then increasingly overflowed and splayed laterally with time. This combination of features shows that the footprint of the current (the area of the ground it occupied), the flow competence (the maximum size of blocks that the current could move), and the runout distance of the block-and-ash flow all increased with time (waxed). The dynamic damage caused by the PDC similarly increased with time.

The thin normal-graded top of the deposit seen at some sites records the final waning flow conditions. The branching distributary lobes of block-and-ash seen on the upper surface of the deposit, for example, near the golf resort, lie far short of the distal tip of the deposit overall, and they show that the distal limit of PDC deposition retreated sourceward with time during the closing, waning phases. The upward transition into stratified ash seen at several sites records (Figure 4e) a late-stage transformation at those sites into fully dilute and turbulent conditions once the lower, more concentrated granular dispersion of the block-and-ash flow had all been deposited.

The lateral thinning and fining of the deposits away from the valley axis are characteristic of block-and-ash flows, which are commonly topographically controlled with axial, channelized thalwegs (Branney & Kokelaar, 2002). However, as the Las Lajas block-and-ash flow waxed and the aggrading deposits gradually filled the alluvial channel, it increasingly spilled out, splaying laterally across the golf course and, 2 km downcurrent of this, overtopped interfluvial into local drainages, most notably on the outside of a marked bend where, as flow conditions waxed, a significant stripped part of the current escaped southwards into a minor catchment (Figure 3) where it partially buried and then battered the village of San Miguel. Where this flow-stripping and overflow event occurred, there is evidence for marked erosional scour, as in crevasse-splay events of turbidity currents (Lang et al., 2021; Piper et al., 2007). Where the current overtopped the interfluvial, standing trees were felled and soil was eroded, leaving longitudinal furrows and partly excavated large alluvial boulders with stoss-side crescent-scours and lee-side gravel tails (Figure 3c; Allen, 1984). Evidently, the overtopping part of the block-and-ash flow was accelerating and erosional. It bypassed the first few hundred meters before encroaching the topography of the new catchment, which caused the flow to funnel and become increasingly depositional with distance downcurrent (Figure 3b). The felled trees were carried 1 km downstream by the flow to the San Miguel village.

The precise timing and emplacement dynamics of the Las Lajas block-and-ash flow is reconstructed from eyewitness accounts collected during the fieldwork, video footages available on the web and deposit characteristics (Figure 11). The main block-and-ash-flow occurred between 2:00 and 3:30 p.m. (local time) and waxed to peak flow conditions between 3:08 and 3:30; that is, 118–140 min after the 1:10 p.m. peak of the eruption. During this relatively short duration, flow became more sustained, as indicated by the lack of evidence within the main deposit for multiple time-breaks, such as traceable stacked flow-units or intercalated ashfall layers deposited during pauses between currents. The rapid escalation (waxing) of the block-and-ash flow after 3:08 p.m. caused the incursion of wider areas (spill over) and the increasing runout and was followed by rapid waning and cessation of flow (Figure 11). The density current was distinctly pulsatory, as reported by eyewitnesses, and recorded by the localized vertical grading patterns in the deposit that indicate the passage of successive pulses with time, including discontinuous scours that record local erosion during waxing phases.

Several eyewitnesses interviewed during the fieldwork report that the PDC first reached Las Lajas bridge on RN-14 at around 2:30 p.m. and that initially it was contained within the ~ 500 m wide river channel. Around 3:00 p.m., the PDC activity there rapidly escalated, and peaked at 3:08 p.m. when onlookers, who had already retreated a few hundreds of meters from the RN-14 bridge since the PDC had arrived, were overwhelmed as the PDC flow path rapidly widened, inundating the entire channel and the road beyond. This suggests that the PDC had started to overtop a topographic barrier above the highway, lateral to the Las Lajas channel.

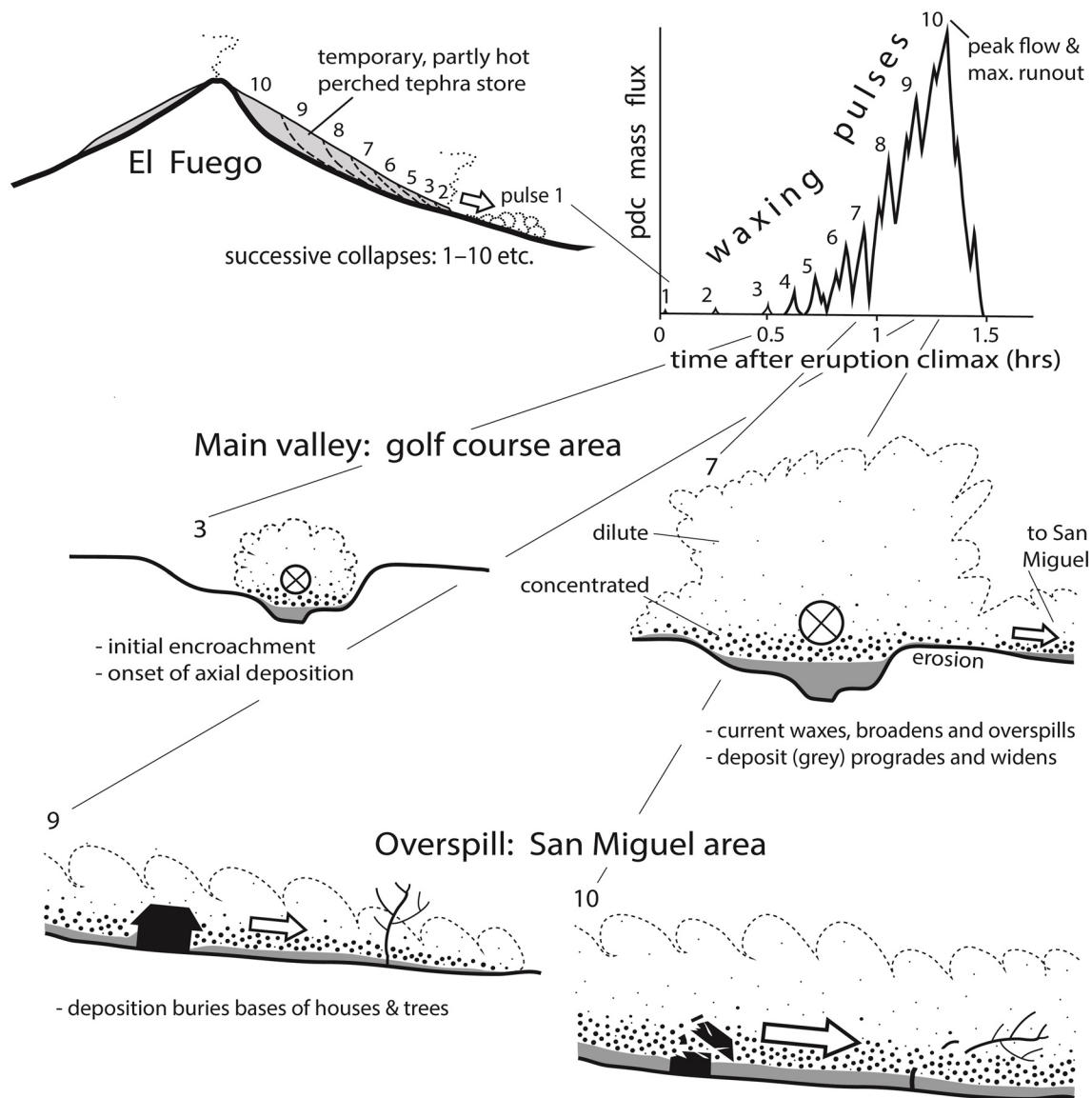


Figure 11. Schematic representation of successive collapses (1–10) of a perched temporary pyroclastic store high on El Fuego volcano, generating a strongly pulsatory deposit-derived pyroclastic density current that waxed overall, was density-stratified (center), aggraded deposits (gray shading) in lower reaches, and then overspilled Las Lajas channel near the golf-course (Figure 3) to flow south directly toward San Miguel de Los Lotes where flow waxed to peak, destroying trees and houses, before rapid waning and cessation. Peak flow conditions occurred 1–1.5 hr after the eruption climax, and did not relate to vent discharge rate.

We infer that the destruction of the Reunion Golf Resort also resulted from the waxing of the PDC, which increasingly could not be contained within the alluvial channel, and so overspilled its banks (Figure 11). The overspilling was also facilitated by deposit aggradation within the channel, reducing the effective height of the channel sides. The main overflow, however, occurred on the southwest bank, where the SSE-trending channel curved eastward just before narrowing to a pinch-point 270 m upstream of the bridge. As the mass flux increased, flow could no longer be contained within the channel at this site and it overflowed on the outside of the bend into the small San Miguel drainage, and followed a more direct path to the village, where its arrival was reported to have happened 10 min after the arrival of the block-and-ash flow at the Las Lajas bridge. This overflow, or partial avulsion, may have been aided by increased SSE momentum as the flow waxed, and also by localized thickening/deepening of the flow as a result of oblique shock (Hákonardóttir & Hogg, 2005) caused by the bend in the channel wall (Hutchison & Dufek, 2021). At the overflow site, the current was highly erosional, leaving longitudinal furrows. Flow-stripping likely occurred, but the deposit facies show that the overspilling part of the current was

granular-fluid-based, not just the upper dilute levels. Such behavior is common in block-and-ash flows elsewhere (e.g., Lube et al., 2011). The internal stratigraphy of the deposit within San Miguel village confirms that the initial PDC arrival there had a relatively low velocity, filling and burying lower parts of houses relatively passively, before a marked increase in flow velocity occurred, with larger blocks transported and greater dynamic destruction of buildings (Figure 11). After this, the PDC activity waned.

5.3.3. Origin of the Flow Unsteadiness

The pulsatory behavior of the 3 June PDCs may have arisen partly by the lateral shifting of bars and braided thalwegs (Branney & Kokelaar, 2002) with entrainment of loose substrate and local avulsions associated with sequential formation and breaching of temporary granular dams and levees (e.g., Jessop et al., 2012; Johnson et al., 2012) as the current waxed, or by the spontaneous development of roll-waves (Viroulet et al., 2018) or “erosion-deposition waves” as produced in experimental sustained granular flows (e.g., Rocha et al., 2019). The resultant pulses in flow competence, velocity, and thickness would cause all granular segregation processes within the PDC's lower, concentrated flow-boundary zone to fluctuate producing various patterns of coarse-tail graded divisions over time (e.g., Figure 5c; c.f. figs 4.5 and 5.8 of Branney & Kokelaar, 2002).

The larger pulses, however, may have derived from successive gravitational failure events as the stored tephra perched on steep slopes high on the volcano collapsed in stages (Figure 11). Progressive failure of granular tephra on slopes can begin with an initial small collapse, this leading to further, larger headwall failures, either in temporal steps (Damiano et al., 2020) or more continuously (Russell et al., 2019; Wang et al., 2016). We envisage that the 3 June 2018 eruption triggered an initial small granular avalanche at the lower edge of the perched pyroclastic store, leaving a small collapse scarp, which being unstable, failed shortly after, this leaving a slightly larger unstable scarp, in turn causing another larger collapse and so on, with successively larger and more frequent collapses that culminated and merged to feed the main block-and-ash-flow about 1.5 hr after the eruption peak. Such a progressive failure mechanism, supplying successively larger batches from the wedge-shaped, upslope-widening, and upslope-thickening perched tephra store (Figure 2), would account for the overall increase in runout distance with time, as each collapse had a larger volume and mass flux than the preceding one. This is consistent also with the waxing T_{emp} recorded by paleomagnetic temperature estimates in the deposit: later failures involved hotter (thicker and more proximal) parts of the tephra store. As the failures bit back to higher elevations toward the summit, the increasing potential energy (fall distance) of successive collapse batches, also may have contributed to the waxing runout distance. Although the duration of each pulse initially may have reflected the duration of the individual granular collapse event, in lower reaches the pulse became prolonged by the funneling effect of the flow as it channeled along the narrow Las Lajas gorge (Figure 1). So as pulses became larger and more frequent, they merged and the pulsatory block-and-ash-flow became more sustained (Figure 11).

6. Perched Temporary Tephra Storage: A New Category of Volcanic Hazard

This study has shown that accumulations of loose tephra on volcanic slopes are prone to rapid re-mobilization, and it is useful to consider the concept of a “*perched temporary tephra store*” (“store” here is used in the sense of storage, not a shop). Key characteristics are an exposed, elevated location, elevated temperature, low strength, and propensity to disaggregate. A tephra store differs from a temporary sediment store (e.g., Syvitski, 1978) in being largely pyroclastic, dry and hot (i.e., $>100^{\circ}\text{C}$), aerated, and containing abundant fine ash: during failure the fine ash is non-cohesive, helps trap air and enhances the mobility of the resultant PDCs.

Perched temporary tephra stores range from segments of gently sloping ignimbrite sheets (e.g., Mount Pinatubo; Torres et al., 1996), stacked pumiceous density current deposits on a fan (e.g., Mount St. Helens; Pallister et al., 2017), to more protracted pyroclastic accumulations from frequent small explosive eruptions on proximal volcanic flanks (e.g., El Fuego, this study). Loose, partly aerated pyroclastic deposits have low strength and, being insulative, may remain hot for several years: loose ignimbrite at Pinatubo remained above 500°C for longer than 2 yr after the 1991 eruption, despite heavy tropical rainfall. Proximal tephra stores may contain interbedded layers of spatter. Tephra with internal bedding that dips in the same direction as the slope, as at El Fuego, is particularly prone to collapse, particularly where it approaches the angle of repose.

To generate a deposit-derived PDC, a perched temporary tephra store must be destabilized: this may happen by continued deposition, this increasing the load or steepening the slope toward repose angle. Heavy rainfall may

add weight by wetting upper parts and changing pore pressures that affect strength. Downslope creep during compaction, slumping, minor collapses, or erosional undercutting by streams or vent-derived pyroclastic currents may cause localized over-steepening. Rapid collapse may be spontaneous or triggered by loading, intrusion, an explosion or seismic shock. When failure happens, PDC ignition is favored by a loose packed, aerated tephra deposit; abundant fine ash content (lowering gas permeability and helps maintain elevated gas pore pressures, partial fluidization, and lowers intergranular friction; Branney & Kokelaar, 2002; Druitt et al., 2007; Phillips et al., 2006); an elevated temperature ($>>100^{\circ}\text{C}$) in order to heat and expand entrained air; pyroclasts that are fragile, friable, angular or thermally stressed so they spall and decrepitate rapidly (e.g., Mellors et al., 1988); a significant topography drop beneath the tephra store; and a landscape morphology that funnels and confines the initial tephra avalanche.

Tall arc volcanoes with steep slopes (stratococones) are a particularly favorable setting for the formation of hazardous perched temporary tephra stores. They generally result from frequent, relatively small-scale eruptions of mafic and intermediate composition. Their apexes typically host thick deposits of loose ash, lapilli, and bombs from Strombolian eruptions, interstratified with layers of spatter (agglutinate) and proximal lavas. Such deposits typically dip close to the angle of repose, and have internal downslope-dipping weaknesses, such as loose tephra layers and autobreccia zones. As they aggrade, they inevitably become gravitationally unstable, particularly when undercut by the headwall advance of erosional gullies. Their instability may be increased further by faulting or tilting during gravitational spreading or magma intrusion, by fumarolic corrosion, seismic shaking, changes in a hydrothermal system, heavy rain, ice-melt, or erosion by lahars or PDCs. Volcanoes liable to generate deposit-derived PDCs include Mayon (Philippines; Moore & Melson, 1969; Rodolfo, 1989), Tungurahua (Ecuador; Hall et al., 2013; Le Pennec et al., 2008), Stromboli (Italy; Di Roberto et al., 2014; Pistolesi et al., 2008; Rosi et al., 2013; Salvatici et al., 2016) and El Fuego (Davies et al., 1978; this work). Most PDC deposits produced at such volcanoes are small volume and hot (Davies et al., 1978; Di Roberto et al., 2014; Nairn & Self, 1978; Yamamoto et al., 2005). Intense fallout of coarse pyroclasts on steep upper slopes of Mount Fuji (Japan) has been invoked to account for avalanching and formation of PDCs that traveled more than 8 km (Yamamoto et al., 2005). Eruption-induced collapse of the flank of a mafic scoria cone perched high on the upper slopes of Etna volcano (Italy), on 11 February 2014, generated a hot deposit-derived PDC that flowed 2.3 km downslope, leaving a lobate granular deposit, ≤ 80 cm thick, surrounded by a thin (3 cm) well-sorted ash layer from a partly buoyant dilute ash plume (Andronico et al., 2018).

The hazard implications of perched temporary tephra storage are not widely appreciated. At El Fuego it is likely that they occurred previously, given the topography and the 2018 Las Lajas block-and-ash flow deposit near the road bridge and San Miguel is underlain by older, similar block-and-ash flow deposits that await further study. Accumulation followed by collapse is liable to repeat. The head of Las Lajas gorge may begin again to fill with tephra.

Frequently active, mildly explosive arc volcanoes should be evaluated for their potential to develop unstable perched temporary tephra storage. Changes in tephra stores could be monitored: some may gradually increase in volume and become increasingly unstable, whereas others may decline through denudation, or equilibrate. Their internal strength may vary as the degree of aeration decreases as the deposits cool and compact, and their mass and elevation may be used to estimate potential PDC runout distances. Heavy rainfall, or oversteepening due to undercutting by streamflow or minor failure may augur an imminent deposit-derived PDC event. Assessment and mitigation of the hazard could involve: (a) examination of satellite footage to identify recent or extant perched tephra stores (Figure 2), or potential sites for their development; (b) combined field and paleomagnetic studies of ancient deposits on the pyroclastic fans, to identify the presence of old deposit-derived PDC deposits, and to assess their geographic extent and their emplacement frequency; (c) stability-modeling of perched granular tephra stores on slopes using DEMs, to identify critical accumulation levels; (d) education and improved awareness of the hazard that temporary tephra stores pose, and the potential for destructive deposit-derived pyroclastic currents. Risk mitigation will be best achieved by planning and timely evacuation. Evaluating the stratigraphy and genesis of both pre-historic and historic deposits is important, drawing on the expertise of field geologists, paleomagnetists and slope stability specialists. As understanding improves, it may become feasible in some instances to artificially trigger controlled collapses using explosives to prevent the growth of a perched tephra store to hazardous dimensions, as is current practice in snow avalanche mitigation (e.g., Simioni & Schweizer, 2018). This could prevent the generation of future longer runout deposit-derived PDCs.

7. Conclusions

Field and thermoremanent magnetization studies of the 3 June 2018, Las Lajas deposits have allowed reconstruction of events prior to, during, and after the 2018 El Fuego disaster with the following conclusions.

1. *Deposit-derived PDCs* are an important volcanic hazard. Their deposits can be distinguished from those of typical vent-derived PDCs, using paleomagnetic data combined with field studies.
2. San Miguel Los Lotes village at El Fuego volcano, Guatemala, was destroyed by a deposit-derived block-and-ash flow that happened more than 1.5 hr after the peak of the 3 June 2018 eruption, at a time when no significant eruptive event was recorded. It is possible that the decline in eruptive activity was one of the reasons why the inhabitants underestimated the risk.
3. In the months and years prior to this, a perched temporary store of partly hot and loose tephra had gradually filled the upper part of Las Lajas gorge during frequent small explosive eruptions. By 3 June, this perched tephra store ranged from cold to over 590°C. About 92% of it had cooled to less than 500°C, as determined by thermoremanent magnetization.
4. The deposit-derived block-and-ash flow generated contained <6% of very hot (potentially juvenile) clasts and was pulsatory, due to rapid progressive (stepped) collapses at source and spontaneous instabilities within the current. It also waxed, causing the geographic footprint and runout distance to increase with time, reaching a peak between 3:10 and 3:30 p.m., when the runout reached 12.2 km.
5. As the Las Lajas alluvial channel started to fill with deposit, the waxing deposit-derived block-and-ash flow increasingly spilled overbank. It spilled south into an adjacent catchment, causing erosion and stripping trees. As the overspill encroached trees and houses it first buried their lower parts and then became more erosional, felling the trees and partly demolishing houses.
6. The hazard implications of perched temporary tephra accumulations have been under-appreciated. Frequently active, mildly explosive volcanoes should be assessed for this hazard, and appropriate mitigation procedures put in place. This should involve sequential satellite, lidar, or visual monitoring of the growth and denudation of perched temporary tephra stores coupled with field and paleomagnetic investigations of pyroclastic fans to assess the frequency and extents of previous deposit-derived PDCs. With improved awareness of this phenomenon internationally, new observatory monitoring practices, and the development of new mitigation procedures, lives may be saved.

Conflict of Interest

The authors declare no conflicts of interest relevant to this study.

Data Availability Statement

Supplementary files are available on <https://doi.org/10.5281/zenodo.5644778>.

Acknowledgments

Fieldwork was coordinated with the Instituto Nacional de Sismología, Vulcanología, Meteorología e Hidrología (INSIVUMEH). The authors thank A. Pineda and G. Laino for the invaluable help in the field and particularly R. Escobar Wolf for discussion on the eruption dynamics. We acknowledge NERC grant NE/S002235/1 to MJB. Thermal demagnetization data used in this work are uploaded to <https://doi.org/10.5281/zenodo.5644778>.

References

- Álvarez-Gómez, J. A., Meijer, P. T., Martínez-Díaz, J. J., & Capote, R. (2008). Constraints from finite element modeling on the active tectonics of northern Central America and the Middle America Trench. *Tectonics*, 27(1). <https://doi.org/10.1029/2007TC002162>
- Albino, F., Biggs, J., Escobar-Wolf, R., Naismith, A., Watson, M., Philips, J. C., & Chigna Marroquin, G. A. (2020). Using TanDEM-X to measure pyroclastic flow source location, thickness, and volume: Application to the 3 June 2018 eruption of Fuego volcano, Guatemala. *Journal of Volcanology and Geothermal Research*, 406, 107063. <https://doi.org/10.1016/j.jvolgeores.2020.107063>
- Allen, J. R. L. (1984). Sedimentary structures: Their character and physical basis. In *Developments in sedimentology* (Vol. 30). Elsevier.
- Andronico, D., Di Roberto, A., De Beni, E., Behncke, B., Bertagnini, A., Del Carlo, P., & Pompilio, M. (2018). Pyroclastic density currents at Etna volcano, Italy: The 11 February 2014 case study. *Journal of Volcanology and Geothermal Research*, 357, 92–105. <https://doi.org/10.1016/j.jvolgeores.2018.04.012>
- Authemayou, C., Brocard, G., Teyssier, C., Simon-Labric, T., Gutiérrez, A., Chiquín, E. N., & Morán, S. (2011). The Caribbean-North America-Cocos triple junction and the dynamics of the Polochic-Motagua fault systems: Pull-up and zipper models. *Tectonics*, 30(3). <https://doi.org/10.1029/2010TC002814>
- Bardot, L. (2000). Emplacement temperature determinations of proximal pyroclastic deposits on Santorini, Greece, and their implications. *Bulletin of Volcanology*, 61, 450–467. <https://doi.org/10.1007/PL00008911>
- Bardot, L., & McClelland, E. (2000). The reliability of emplacement temperature estimates using paleomagnetic methods: A case study from Santorini, Greece. *Geophysical Journal International*, 143, 39–51. <https://doi.org/10.1046/j.1365-246x.2000.00186.x>
- Berlo, K., Stix, J., Roggensack, K., & Ghaleb, B. (2012). A tale of two magmas, Fuego, Guatemala. *Bulletin of Volcanology*, 74(2), 377–390. <https://doi.org/10.1007/s00445-011-0530-8>

- Boletín Vulcanológico Especial. *BEFGO #29-2018, Guatemala 03 de Junio 2018, 13:45, Hora Local*. Retrieved from <https://insivumeh.gob.gt/>
- Branney, M. J., Brown, R. J., & Calder, E. (2021). Pyroclastic rocks. In D. Alderton & S. A. Elias (Eds.), *Encyclopedia of geology* (2nd ed., Vol. 2, pp. 277–300). Academic Press. <https://doi.org/10.1016/b978-0-08-102908-4.00103-x>
- Branney, M. J., & Kokelaar, P. (2002). *Pyroclastic density currents and the sedimentation of ignimbrites* (Vol. 27, p. 142). Geological Society.
- Breard, E. C. P., & Lube, G. (2017). Inside pyroclastic density currents—Uncovering the enigmatic flow structure and transport behavior in large-scale experiments. *Earth and Planetary Science Letters*, 458, 22–36. <https://doi.org/10.1016/j.epsl.2016.10.016>
- Brown, R. J., & Branney, M. J. (2004). Bypassing and diachronous deposition from density currents: Evidence from a giant regressive bed form in the Poris ignimbrite, Tenerife, Canary Islands. *Geology*, 32, 445–448. <https://doi.org/10.1130/g20188.1>
- Brown, S. K., Jenkins, S. F., Sparks, R. S. J., Odbert, H., & Auker, M. R. (2017). Volcanic fatalities database: Analysis of volcanic threat with distance and victim classification. *Journal of Applied Volcanology*, 6, 15. <https://doi.org/10.1186/s13617-017-0067-4>
- Buesch, D. C. (1992). Incorporation and redistribution of locally derived lithic fragments within a pyroclastic flow. *The Geological Society of America Bulletin*, 104(9), 1193–1207. [https://doi.org/10.1130/0016-7606\(1992\)104<1193:iarold>2.3.co;2](https://doi.org/10.1130/0016-7606(1992)104<1193:iarold>2.3.co;2)
- Bursik, M., & Woods, A. (1996). The dynamics and thermodynamics of large ash flows. *Bulletin of Volcanology*, 58, 175–193. <https://doi.org/10.1007/s004450050134>
- Calder, E. S., Sparks, R. S. J., & Gardeweg, M. C. (2000). Erosion, transport, and segregation of pumice and lithic clasts in pyroclastic flow inferred from ignimbrite at Lascar Volcano, Chile. *Journal of Volcanology and Geothermal Research*, 104(1–4), 201–235. [https://doi.org/10.1016/s0377-0273\(00\)00207-9](https://doi.org/10.1016/s0377-0273(00)00207-9)
- Cioni, R., Gurioli, L., Lanza, R., & Zanella, E. (2004). Temperatures of the CE 79 pyroclastic density current deposits (Vesuvius, Italy). *Journal of Geophysical Research: Solid Earth*, 109, B02207. <https://doi.org/10.1029/2002JB002251>
- Cole, P. D., Calder, E. S., Druitt, T. H., Hoblitt, R., Robertson, R., Sparks, R. S. J., & Young, S. R. (1998). Pyroclastic flows generated by gravitational instability of the 1996–97 lava dome of Soufriere Hills volcano, Montserrat. *Geophysical Research Letters*, 25(18), 3425–3428. <https://doi.org/10.1029/98gl01510>
- Cole, R. P., Ohneiser, C., White, J. D. L., Townsend, D. B., & Leonard, G. S. (2019). Paleomagnetic evidence for cold emplacement of eruption-fed density current deposits beneath an ancient summit glacier, Tongariro volcano, New Zealand. *Earth and Planetary Science Letters*, 522, 155–165. <https://doi.org/10.1016/j.epsl.2019.07.004>
- Damiano, E., Darban, R., Olivares, L., & Picarelli, L. (2020). *An investigation of progressive failure in granular slopes leading to flow-like landslides. SCG-XIII Intern. Symposium on Landslides. Cartagena, Columbia—15–19 June 2020*. International Society for Soil Mechanics and Geotechnical Engineering.
- Davies, D. K., Quearry, M. W., & Bonis, S. B. (1978). Glowing avalanches from the 1974 eruption of the volcano Fuego, Guatemala. *The Geological Society of America Bulletin*, 89(3), 369–384. [https://doi.org/10.1130/0016-7606\(1978\)89<369:gaftoe>2.0.co;2](https://doi.org/10.1130/0016-7606(1978)89<369:gaftoe>2.0.co;2)
- Di Roberto, A., Bertagnini, A., Pompilio, M., & Bisson, M. (2014). Pyroclastic density currents at Stromboli volcano (Aeolian Islands, Italy): A case study of the 1930 eruption. *Bulletin of Volcanology*, 76(6), 1–14. <https://doi.org/10.1007/s00445-014-0827-5>
- Druitt, T. H. (1998). Pyroclastic density currents. In J. S. Gilbert & R. S. J. Sparks (Eds.), *The physics of explosive volcanic eruptions* (Vol. 145, pp. 145–182). Geological Society, London, Special Publications. <https://doi.org/10.1144/gsl.sp.1996.145.01.08>
- Druitt, T. H., Avard, G., Bruni, G., Letteri, P., & Maez, F. (2007). Gas retention in fine-grained pyroclastic flow materials at high temperatures. *Bulletin of Volcanology*, 69, 881–901. <https://doi.org/10.1007/s00445-007-0116-7>
- Dualeh, E. W., Ebmeier, S. K., Wright, T. J., Albino, F., Naismith, A., Biggs, J., et al. (2021). Analyzing explosive volcanic deposits from satellite-based radar backscatter, Volcán de Fuego, 2018. *Journal of Geophysical Research: Solid Earth*, 126, e2021JB022250. <https://doi.org/10.1029/2021JB022250>
- Escobar Wolf, R. P. (2013). *Volcanic processes and human exposure as elements to build a risk model for Volcan de Fuego* (Unpublished dissertation) (p. 216). Guatemala: Michigan Technological University. Retrieved from <https://digitalcommons.mtu.edu/etds/638>
- Farin, M., Mangene, A., & Roche, O. (2013). Fundamental changes of granular flow dynamics, deposition, and erosion processes at high slope angles: Insights from laboratory experiments. *Journal of Geophysical Research: Earth Surface*, 119(3), 504–532.
- Fisher, R. V. (1977). Erosion by volcanic base-surge density currents—U-shaped channels. *The Geological Society of America Bulletin*, 88, 1287–1297. [https://doi.org/10.1130/0016-7606\(1977\)88<1287:ebvdc>2.0.co;2](https://doi.org/10.1130/0016-7606(1977)88<1287:ebvdc>2.0.co;2)
- Global Volcanism Program. (2018). In E. Venzke (ed.), [Fuego (342090)] in *Volcanoes of the World*, v. 4.6.7. Smithsonian Institution. Retrieved from <https://volcano.si.edu/volcano.cfm?vn=342090>
- Guinn, N. K., Gardner, J. E., & Helper, M. A. (2022). Dynamic pressure evolution within the 18 May 1980 Mount St. Helens pyroclastic density current: Evidence from tree damage. *Bulletin of Volcanology*, 84(4), 1–12. <https://doi.org/10.1007/s00445-022-01548-6>
- Hákonardóttir, K. M., & Hogg, A. J. (2005). Oblique shocks in rapid granular flows. *Physics of Fluids*, 17, 077101. <https://doi.org/10.1063/1.1950688>
- Hall, M. L., Steele, A. L., Mothes, P. A., & Ruiz, M. C. (2013). Pyroclastic density currents (PDC) of the 16–17 August 2006 eruptions of Tungurahua volcano, Ecuador: Geophysical registry and characteristics. *Journal of Volcanology and Geothermal Research*, 265, 78–93. <https://doi.org/10.1016/j.jvolgeores.2013.08.011>
- Heerema, K., Talling, P., Cartigny, M. J., Paull, C. K., Bailey, L., Simmons, S. M., et al. (2020). What determines the downstream evolution of turbidity currents? *Earth and Planetary Science Letters*, 532, 11023. <https://doi.org/10.1594/IEDA/32529>
- Hutchison, K. A., & Dufek, J. (2021). Generation of overspill pyroclastic density currents in sinuous channels. *Journal of Geophysical Research: Solid Earth*, 126, E2021JB122442. <https://doi.org/10.1029/2021JB122442>
- Instituto Nacional de Sismología, Vulcanología, Meteorología e Hidrología (INSIVUMEH). (2012a). *Folleto sobre Volcán de Fuego*. Retrieved from <http://www.insivumeh.gob.gt>
- Instituto Nacional de Sismología, Vulcanología, Meteorología e Hidrología (INSIVUMEH). (2012b). *Reporte preliminar de la erupción del Volcán de Fuego 13 de septiembre 2012*. Retrieved from http://www.insivumeh.gob.gt/folletos/REPORTE_ERUPCION_DE_FUEGO_13_SEP_2012_%28OK%29.pdf
- Jessop, D. E., Kelfoun, K., Labazuy, P., Mangeny, A., Roche, O., Tillier, J. L., et al. (2012). LiDAR derived morphology of the 1993 Lascar pyroclastic flow deposits, and implication for flow dynamics and rheology. *Journal of Volcanology and Geothermal Research*, 245, 81–97. <https://doi.org/10.1016/j.jvolgeores.2012.06.030>
- Jobe, Z. R., Lowe, D. R., & Morris, W. R. (2012). Climbing-ripple successions in turbidite systems: Depositional environments, sedimentation rates, and accumulation times. *Sedimentology*, 59, 867–898. <https://doi.org/10.1111/j.1365-3091.2011.01283.x>
- Johnson, C. G., Kokelaar, B. P., Iverson, R. M., Logan, M., LaHusen, R. G., & Gray, J. M. N. T. (2012). Grain-size segregation and levee formation in geophysical mass flows. *Journal of Geophysical Research: Solid Earth*, 117, F01032. <https://doi.org/10.1029/2011JF00218510>
- Kelfoun, K. (2017). A two-layer depth averaged model for both the dilute and the concentrated parts of pyroclastic currents. *Journal of Geophysical Research: Solid Earth*, 122(6), 4293–4311. <https://doi.org/10.1002/2017JB014013>

- Kieffer, S. W., Meiburg, E., Best, J., & Austin, J. (2021). Mysterious grooves of Volcán Bárcena: A review of the role of streamwise counter-rotating vortices during eruption by dilute pyroclastic density currents. *Bulletin of Volcanology*, 83, 26. <https://doi.org/10.1007/s00445-021-01440-9>
- Kirschvink, J. L. (1980). The least squares line and plane and the analysis of paleomagnetic data. *Geophysical Journal International*, 62(3), 699–718. <https://doi.org/10.1111/j.1365-246x.1980.tb02601.x>
- Kurtz, A. W. (1913). Documentos Antiguos: Copia de dos cartas manuscritas de Don Pedro de Alvarado a Hernando Cortes, 11 de abril y 28 de julio 1524. Tip.–Arenaleshijos. Retrieved 12 July 2018 from <https://www.scribd.com/doc/213352772/Cartas-de-Pedro-de-Alvarado-a-Hernando-Cortes>
- Lang, J., Fedele, J. J., & Hoyal, D. C. J. D. (2021). Three-dimensional submerged wall jets and their transition to density flows—Morphodynamics and implications for the depositional record. *Sedimentology*, 68(4), 1297–1327.
- Le Pennec, J.-L., Jaya, D., Samaniego, P., Ramón, P., Moreno, S., Egred, J., & van der Plicht, J. (2008). The CE 1300–1700 eruptive periods at Tungurahua volcano, Ecuador, revealed by historical narratives, stratigraphy, and radiocarbon dating. *Journal of Volcanology and Geothermal Research*, 176, 70–81. <https://doi.org/10.1016/j.jvolgeores.2008.05.019>
- Lesti, C., Porreca, M., Giordano, G., Mattei, M., Cas, R. A. F., Wright, H. M. N., et al. (2011). High-temperature emplacement of the Cerro Galán and Toconquis Group ignimbrites (Puna plateau, NW Argentina) determined by TRM analyses. *Bulletin of Volcanology*, 73, 1535–1565. <https://doi.org/10.1007/s00445-011-0536-2>
- Lube, G., Cronin, S. J., & Thouret, J. C. (2011). Kinematic characteristics of pyroclastic density currents at Merapi and controls of their avulsion from natural and engineered channels. *The Geological Society of America Bulletin*, 123, 1127–1140. <https://doi.org/10.1130/b30244.1>
- Lyons, J. J., Waite, G. P., Rose, W. L., & Chigna, G. (2010). Patterns in open vent, Strombolian behavior at Fuego volcano, Guatemala, 2005–2007. *Bulletin of Volcanology*, 72(1), 1. <https://doi.org/10.1007/s00445-009-0305-7>
- Mangeny, A., Roche, O., Hungr, O., Mangold, N., Faccanoni, G., & Lucas, A. (2010). Erosion and mobility in granular collapse over sloping beds. *Journal of Geophysical Research*, 115(F3), F03040. <https://doi.org/10.1029/2009jf001462>
- Marti, J. J., Diez-Gil, J. L., & Ortiz, R. (1991). Conduction model for the thermal influence of lithic clasts in mixtures of hot gases and ejecta. *Journal of Geophysical Research*, 96(B13), 21879–21885. <https://doi.org/10.1029/91jb02149>
- McClelland, E. A., & Druitt, T. H. (1989). Paleomagnetic estimates of emplacement temperatures of pyroclastic deposits on Santorini, Greece. *Bulletin of Volcanology*, 51, 16–27. <https://doi.org/10.1007/bf01086758>
- McClelland, E. A., Wilson, C. J. N., & Bardot, L. (2004). Paleotemperature determinations for the 1.8 ka Taupo ignimbrite, New Zealand, and implications for the emplacement history of a high-velocity pyroclastic flow. *Bulletin of Volcanology*, 66, 492–513. <https://doi.org/10.1007/s00445-003-0335-5>
- Mellors, R. A., Waite, R. B., & Swanson, D. A. (1988). Generation of pyroclastic flows and surges by hot rock avalanches from the dome of Mount St Helens volcano, USA. *Bulletin of Volcanology*, 50, 14–25. <https://doi.org/10.1007/bf01047505>
- Moore, J. G., & Melson, W. J. (1969). Nuées Ardentes of the 1968 eruption of Mayon Volcano, Philippines. *Bulletin of Volcanology*, 33, 600. <https://doi.org/10.1007/bf02596528>
- Nairn, I. A., & Self, S. (1978). Explosive eruptions and pyroclastic avalanches from Ngauruhoe in February 1975. *Journal of Volcanology and Geothermal Research*, 3(1–2), 39–60. [https://doi.org/10.1016/0377-0273\(78\)90003-3](https://doi.org/10.1016/0377-0273(78)90003-3)
- Naismith, A. K., Watson, I. M., Escobar-Wolf, R., Chigna, G., Thomas, H., Coppola, D., & Chun, C. (2019). Eruption frequency patterns through time for the current (1999–2018) activity cycle at Volcán de Fuego derived from remote sensing data: Evidence for an accelerating cycle of explosive paroxysms and potential implications of eruptive activity. *Journal of Volcanology and Geothermal Research*, 371, 206–219. <https://doi.org/10.1016/j.jvolgeores.2019.01.001>
- Pallister, J. S., Clynne, M. A., Wright, H. M., Van Eaton, A. R., Vallance, J. W., Sherrod, D. R., & Kokelaar, B. P. (2017). *Field-trip guide to Mount St. Helens, Washington—An overview of the eruptive history and petrology, tephra deposits, 1980 pyroclastic density current deposits, and the crater* (p. 65). U.S. Geological Survey Scientific Investigations Report 2017–5022–D. <https://doi.org/10.3133/sir2017502D>
- Pardini, F., Queißer, M., Naismith, A., Watson, I. M., Clarisse, L., & Burton, M. R. (2019). Initial constraints on triggering mechanisms of the eruption of Fuego volcano (Guatemala) from 3 June 2018 using IASI satellite data. *Journal of Volcanology and Geothermal Research*, 376, 54–61. <https://doi.org/10.1016/j.jvolgeores.2019.03.014>
- Paterson, G. A., Roberts, A. P., Mac Niocaill, C., Muxworthy, A. R., Gurioli, L., Viramonté, J. G., et al. (2010). Paleomagnetic determination of emplacement temperatures of pyroclastic deposits: An under-utilized tool. *Bulletin of Volcanology*, 72, 309–330. <https://doi.org/10.1007/s00445-009-0324-4>
- Patrick, M. R., Harris, A. J., Ripepe, M., Dehn, J., Rothery, D. A., & Calvari, S. (2007). Strombolian explosive styles and source condition: Insights from thermal (FLIR) video. *Bulletin of Volcanology*, 69(7), 769–784. <https://doi.org/10.1007/s00445-006-0107-0>
- Pérez-Rodríguez, N., Morales, J., Goguitchaichvili, A., & García-Tenorio, F. (2019). A comprehensive paleomagnetic study from the last Plinian eruptions of Popocatepetl volcano: Absolute chronology of lavas and estimation of emplacement temperatures of PDCs. *Earth Planets and Space*, 71, 80. <https://doi.org/10.1186/s40623-019-1059-x>
- Phillips, J. C., Hogg, A. J., Kerswell, R. R., & Thomas, N. H. (2006). Enhanced mobility of granular mixtures of fine and coarse particles. *Earth and Planetary Science Letters*, 246, 466–480. <https://doi.org/10.1016/j.epsl.2006.04.007>
- Piper, D. J., Shaw, J., & Skene, K. I. (2007). Stratigraphic and sedimentological evidence for late Wisconsinan sub-glacial outburst floods to Laurentian Fan. *Paleogeography, Paleoclimatology, Paleoecology*, 246(1), 101–119. <https://doi.org/10.1016/j.palaeo.2006.10.029>
- Pistolesi, M., Rosi, M., Pioli, L., Renzulli, A., Bertagnini, A., & Andronico, D. (2008). The paroxysmal event and its deposits. In S. Calvari, S. Inguaggiato, G. Puglisi, M. Ripepe, & M. Rosi (Eds.), *Stromboli volcano: An integrated study of the 2002–2003 eruption* (pp. 317–330). Washington, USA: American Geophysical Union.
- Porreca, M., Mattei, M., MacNiocaill, C., Giordano, G., McClelland, E., & Funicello, R. (2008). Paleomagnetic evidence for low-temperature emplacement of the phreatomagmatic Peperino Albano ignimbrite (Colli Albani volcano, Central Italy). *Bulletin of Volcanology*, 70, 877–893. <https://doi.org/10.1007/s00445-007-0176-8>
- Rocha, F. M., Johnson, C. G., & Gray, J. M. N. T. (2019). Self-channelisation and levee formation in monodisperse granular flows. *Journal of Fluid Mechanics*, 876, 591–641. <https://doi.org/10.1017/jfm.2019.518>
- Roche, O., Azzaoui, N., & Guillin, A. (2021). Discharge rate of explosive volcanic eruption controls runout distance of pyroclastic density currents. *Earth and Planetary Science Letters*, 568, 117017. <https://doi.org/10.1016/j.epsl.2021.117017>
- Roche, O., Niño, Y., Mangeny, A., Brand, B., Pollock, N., & Valentine, G. A. (2013). Dynamic pore-pressure variations induce substrate erosion by pyroclastic flows. *Geology*, 41(10), 1107–1110. <https://doi.org/10.1130/g34668.1>
- Rodolfo, K. S. (1989). Origin and early evolution of lahar channel at Mabinit. *Geological Society of America Bulletin*, 101, 414–426. [https://doi.org/10.1130/0016-7606\(1989\)101\(0414:oaeool\)2.3.co;2](https://doi.org/10.1130/0016-7606(1989)101(0414:oaeool)2.3.co;2)
- Rose, W. I., Jr., Anderson, A. T., Jr., Woodruff, L. G., & Bonis, S. B. (1978). The October 1974 basaltic tephra from Fuego volcano: Description and history of the magma body. *Journal of Volcanology and Geothermal Research*, 4(1–2), 3–53. [https://doi.org/10.1016/0377-0273\(78\)90027-6](https://doi.org/10.1016/0377-0273(78)90027-6)

- Rose, W. I., Self, S., Murrow, P. J., Bonadonna, C., Durant, A. J., & Ernst, G. G. J. (2008). Nature and significance of small volume fall deposits at composite volcanoes: Insights from the 14 October 1974 Fuego eruption, Guatemala. *Bulletin of Volcanology*, *70*(9), 1043–1067. <https://doi.org/10.1007/s00445-007-0187-5>
- Rosi, M., Pistolesi, M., Bertagnini, A., Landi, P., Pompilio, M., & Di Roberto, A. (2013). Stromboli volcano, Aeolian Islands (Italy): Present eruptive activity and hazards. *Geological Society, London, Memoirs*, *37*(1), 473–490. <https://doi.org/10.1144/m37.14>
- Rowley, P. D., Kuntz, M. A., & MacLeod, N. S. (1981). Pyroclastic-flow deposits. In P. W. Lipman, & D. R. Mullineaux (Eds.), *The 1980 eruptions of Mount St. Helens* (Vol. 1250, pp. 489–512). U.S. Geological Survey Professional Paper.
- Russell, A. S., Johnson, C. G., Edwards, A. N., Viroulet, S., Rocha, F. M., & Gray, J. M. N. T. (2019). Retrogressive failure of a static granular layer on an inclined plane. *Journal of Fluid Mechanics*, *869*, 313–340. <https://doi.org/10.1017/jfm.2019.215>
- Salvatici, T., Di Roberto, A., Di Traglia, F., Bisson, M., Morelli, S., Fidolini, F., et al. (2016). From hot rocks to glowing avalanches: Numerical modeling of gravity-induced pyroclastic density currents and hazard maps at the Stromboli volcano (Italy). *Geomorphology*, *273*, 93–106. <https://doi.org/10.1016/j.geomorph.2016.08.011>
- Scott, K. M. (1988). *Lahars and lahar-runout flows in the Toutle-Cowlitz River system*. Washington. U.S. Geological Survey, Professional Paper, (1447-A, p. 83).
- Shimizu, H. A., Koyaguchi, T., & Suzuki, Y. J. (2019). The run-out distance of large-scale pyroclastic density currents: A two-layer depth-averaged model. *Journal of Volcanology and Geothermal Research*, *381*, 168–184. <https://doi.org/10.1016/j.jvolgeores.2019.03.013>
- Simioni, S., & Schweizer, J. (2018). *Methods of artificial avalanche triggering: Gas vs. solid explosives*. Proceedings, International Snow Science Workshop, Innsbruck, Austria. (pp. 158–161).
- Sparks, R. S. J., Gardeweg, M. C., Calder, E. S., & Matthews, S. J. (1997). Erosion by pyroclastic flows on Lascar volcano, Chile. *Bulletin of Volcanology*, *58*, 557–565. <https://doi.org/10.1007/s004450050162>
- Suzuki-Kamata, K. (1988). The ground layer of Ata pyroclastic flow deposit, southwestern Japan—Evidence for the capture of lithic fragments. *Bulletin of Volcanology*, *50*(2), 119–129. <https://doi.org/10.1007/bf01275173>
- Syvitsky, J. P. M. (1978). Sediment fluxes and rates of sedimentation. In G. V. Middleton, M. J. Church, M. Coniglio, L. A. Hardie, & F. J. Longstaffe (Eds.), *Encyclopedia of sediments and sedimentary rocks*. Springer. https://doi.org/10.1107/978-1-4020-3609-5_180
- Torres, R. C., Self, S., & Martinez, M. L. (1996). Secondary pyroclastic flows from the 15 June 1991, ignimbrite of Mount Pinatubo. In C. G. Newhall, & S. Punongbayan (Eds.), *Fire and mud: Eruptions of Mount Pinatubo, Philippines* (pp. 665–678). Philippine Institute of Volcanology and Seismology, Quezon City, University of Washington Press.
- Trolese, M., Giordano, G., Cifelli, F., Winkler, A., & Mattei, M. (2017). Forced transport of thermal energy in magmatic and phreatomagmatic large volume ignimbrites: Paleomagnetic evidence from the Colli Albani volcano, Italy. *Earth and Planetary Science Letters*, *478*, 179–191. <https://doi.org/10.1016/j.epsl.2017.09.004>
- Turner, G. M., Alloway, B. V., Dixon, B. J., & Atkins, C. B. (2018). Thermal history of volcanic debris flow deposits on the eastern flanks of Mt. Taranaki, New Zealand: Implications for future hazards. *Journal of Volcanology and Geothermal Research*, *353*, 55–67. <https://doi.org/10.1016/j.jvolgeores.2018.01.017>
- Uehara, D., Cas, R. A. F., Folkes, C., Takarada, S., Oda, H., & Porreca, M. (2015). Using thermal remanent magnetization (TRM) to distinguish block and ash flow and debris flow deposits, and to estimate their emplacement temperature: 1991–1995 lava dome eruption at Mt. Unzen volcano, Japan. *Journal of Volcanology and Geothermal Research*, *303*, 92–111. <https://doi.org/10.1016/j.jvolgeores.2015.07.019>
- Viroulet, S., Baker, J. L., Rocha, F. M., Johnson, C. G., Kokelaar, B. P., & Grey, J. M. N. T. (2018). The kinematics of bidisperse granular roll waves. *Journal of Fluid Mechanics*, *848*, 836–875. <https://doi.org/10.1017/jfm.2018.348>
- Waite, G. P., Nadeau, P. A., & Lyons, J. J. (2013). Variability in eruption style and associated very long period events at Fuego volcano, Guatemala. *Journal of Geophysical Research: Solid Earth*, *118*(4), 1526–1533. <https://doi.org/10.1002/jgrb.50075>
- Walker, G. P. L., Self, S., & Froggatt, P. C. (1981). The ground layer of the Taupo ignimbrite: A striking example of sedimentation from a pyroclastic flow. *Journal of Volcanology and Geothermal Research*, *10*, 1–11. [https://doi.org/10.1016/0377-0273\(81\)90051-2](https://doi.org/10.1016/0377-0273(81)90051-2)
- Wang, B., Vardon, P. J., & Hicks, M. A. (2016). Investigation of retrogressive and progressive slope failure mechanisms using the material point method. *Computers and Geotechnics*, *78*, 88–98. <https://doi.org/10.1016/j.compgeo.2016.04.016>
- Williams, R., Branney, M. J., & Barry, T. L. (2014). Temporal and spatial evolution of a waxing then waning catastrophic density current revealed by chemical mapping. *Geology*, *42*(2), 107–110. <https://doi.org/10.1130/g34830.1>
- Wilson, C. J. N. (1985). The Taupo eruption, New Zealand II. The Taupo ignimbrite. *Philosophical Transactions of the Royal Society A*, *314*, 229–310. <https://doi.org/10.1098/rsta.1985.0020>
- Yamamoto, T., Takada, A., IshizukaMiyaji, Y. N., & Tajima, Y. (2005). Basaltic pyroclastic flows of Fuji volcano, Japan: Characteristics of the deposits and their origin. *Bulletin of Volcanology*, *67*, 622. <https://doi.org/10.1007/s00445-004-0398-y>
- Zanella, E., Sulpizio, R., Gurioli, L., & Lanza, R. (2015). *Temperatures of the pyroclastic density currents deposits emplaced in the last 22 kyr at Somma-Vesuvius (Italy)* (Vol. 396, pp. 13–33). Geological Society of London Special Publications. <https://doi.org/10.1144/sp396.4>
- Zijderveld, J. D. A. (1967). AC demagnetization of rocks: Analysis of results. In D. W. Collinson, K. M. Creer, & S. K. Runcorn (Eds.), *Methods in paleomagnetism* (pp. 254–286). Elsevier.